TECHNISCHE UNIVERSITÄT WIEN

DIPLOMARBEIT

Monitoring Coastal Erosion in Arctic Regions with SAR Data

zur Erlangung des akademischen Grades

Diplom-Ingenieurin

im Rahmen des Studiums

Geodäsie und Geoinformation

eingereicht von

Sarah Ley
Matrikelnummer 1241427

ausgeführt am Institut für Geodäsie und Geoinformation
der Fakultät für Mathematik und Geoinformation der Technischen Universität Wien

Betreuung
Betreuer/in: Privatdoz. Dipl.-Geograf Dr. Annett Bartsch

Wien, 06.09.2019

(Unterschrift Verfasser/in) (Unterschrift Betreuer/in)

Abstract

The annual coastal erosion rates of Arctic coasts are among the highest in the world, and the rates are increasing because of climate change. Monitoring of these mass movements with optical images is challenging due to frequent cloud cover of the Arctic. Synthetic Aperture Radars (SAR) are barely affected by the atmosphere, but the commonly used interferometry methods are not effective for the rapidly changing Arctic coastline. Therefore researchers introduced a backscatter-threshold based method with high-resolution TerraSAR-X images. The aim of this study was to advance SAR data analysis for coastal erosion measurements. Therefore, this study applies threshold classification to a variety of Arctic SAR images. TerraSAR-X X-band, PALSAR and PALSAR-2 L-band, and Sentinel-1 C-band ellipsoid corrected images were analyzed. The images had spatial resolutions of 0.62 to 20 m and various polarizations. The thresholds were tested with and without filtering in study areas along the Yukon Coast, the Bykovsky Peninsula, and the Barents Sea Coast. The analysis showed only weak effects of the incidence angle on the backscatter. All sample distributions were modeled well with linear threshold functions. During the error assessment all steep coast test samples were classified correctly by the threshold functions (100% producer's accuracy). Misclassification of land and water occurred for all threshold functions. Overall, the threshold functions for filtered, co-polarized images had a slightly higher classification accuracy, with Kappa Coefficients between 83.52% and 99.84%. Misclassifications were mainly caused by wet snow, wide sand beaches, and infrastructure. The classification results were further used to calculate seasonal, annual, and multi-year coastline change rates. The coastline was identified based on steep cliff classifications or the border between water and land classifications. For regions near Kay Point on the Yukon Coast, the near-zero calculated seasonal and annual shoreline change rates matched optical indications that erosion processes are not active in that area. For the west coast of Herschel Island, erosion rates calculated based on steep cliff classifications matched results of previous studies and optical images. However, the erosion estimates from land–water boundary did not match well, probably because snow interfered with the land classification. The annual and multi-year land–water rates for a region at the Barents Seas Coast showed good accordance with previous estimates. A comparison between the annual and multi-annual results based on steep coast classifications showed overall the same coastline movement tendencies. Greater differences become apparent when the results are split into smaller areas, which could be because of the high uncertainty of the annual rates or changes of the erosion processes over the years. Annual results for same regions are similar but not identical because of high rate uncertainties and possibly small differences between the chosen transects and orbit parameters of the compared images.

Kurzfassung

Arktische Küsten haben eine der höchsten Erosionsraten der Welt. Dies wird durch den Klimawandel noch weiter versärkt. Aufgrund der starken Bewölkung der Arktis ist die Überwachung dieser Massenbewegungen mit optischen Daten schwierig. Synthetische Apertur Radare (SAR) bieten eine Alternative, da sie kaum durch die Atmosphäre beeinflusst werden. Interferometrie Methoden können jedoch aufgrund der großen Änderungsraten nicht angewandt werden, weswegen eine Rückstreuungs-Schwellenwert Klassifikationsmethode eingeführt wurde. Ziel dieser Arbeit war es, die SAR Datenanalyse für arktische Küstenerosion zu verbessen. Dazu wurden einfallswinkelabhängige Rückstreuungs-Schwellenwertfunktionen zur Klassifikation von SAR Daten verschiedener Wellenlängen verwendet. Für die Analyse wurden TerraSAR-X X-Band, PALSAR und PALSAR-2 L-Band und Sentinel-1 C-Band Ellipsoid korrigierte Daten mit einer räumlichen Auflösung von 0,62 bis 20 m verwendet. Die Schwellenwertfunktionen wurden mit gefilterten und ungefilterten Daten für Untersuchungsgebiete entlang der Yukon Küste, der Bykovsky Halbinsel und der Barentssee Küste getestet. Nur ein geringer Einfluss des Einfallswinkels auf die Rückstreuungswerte konnte festgestellt werden. Auf Grundlage der Stichprobenverteilung wurden lineare Schwellenwertfunktionen gewählt. Während der Fehleranalyse wurden alle Steilküsten Stichproben korrekt als Steilküste klassifiziert. Fehlklassifikationen zwischen den Land und Wasser Klassen waren für alle Schwellenwertfunktionen zu beobachten. Insgesamt wurde die höchste Klassifikationsgenauigkeit (Kappa Koeffizienten zwischen 83,52% und 99,84%) für co-polarisierte, gefilterte Daten erreicht. Fehlklassifikationen wurden hauptsächlich durch nassen Schnee, glatte Sandebenen und Infrastruktur verursacht. Die Klassifikationsergebnisse wurden anschließend verwendet um saisonale, jährliche und mehrjährige Küstenerosionsraten zu berechnen. Die Küstenlinien wurden auf Grundlage der Steilküsten Klassifikation oder der Grenze zwischen den Land und Wasser Klassen definiert. Für die Regionen nähe Kay Point an der Yukon Küste stimmten die berechneten Erosionsraten nahe Null mit den optischen Indikatoren überein, dass die Erosionsprozesse in diesem Gebiet nicht sehr ausgeprägt sind. Die auf Steilküsten Klassifikationen basierenden, errechneten Raten der Westküste der Insel Herschel entsprachen den Ergebnissen anderer Studien und optischen Bildern. Die auf der Land-Wasser Grenze basierenden Ergebnisse stimmten nicht überein. Dies ist vermutlich auf Schnee Fehlklassifikationen zurückzuführen. Die jährlichen und mehrjährigen Erosionsraten der Barentsee Küste, basierend auf der Land-Wasser Grenze, zeigten gute Übereinstimmung mit früheren Schätzungen. Ein genereller Vergleich der jährlichen und mehrjährigen Raten, basierend auf Steilküsten Klassifikationen, zeigt dieselben Erosionstendenzen. Bei einem genaueren Vergleich der Ergebnisse werden jedoch Unterschiede zwischen den Raten kleinerer Küstenabschnitte deutlich.

Dies kann durch die große Messunsicherheit der jährlichen Raten bedingt sein. Die jährlichen Raten für dieselben Regionen zeigen große Übereinstimmungen, sind jedoch nicht identisch. Auch dies kann durch die große Messunsicherheit der jährlichen Raten oder kleine Unterschiede zwischen den untersuchten Abschnitten oder den Bahnparametern der verglichenen Daten bedingt sein.

Acknowledgements

I first want to thank my supervisor Dr. Annett Bartsch for the opportunity to combine my thesis with an internship at her company b.geos. She always found time to answer my questions and gave me useful feedback.

I also want to thank Georg Pointner for answering my numerous Python related questions and providing the raster-to-polygon script cited in Section 4.3.1.

I am very grateful for all the help and support my boyfriend Aaron has given me. He fed me, showed patience, calmed me down in stressful moments, and explained the Oxford comma several times. I don't know what I would have done without him.

A special thanks goes to my friends, especially Melanie for listening to all the boooooring thesis related stories of mine. I'm not sure how she survived that.

Zum Schluss möchte ich meinen Eltern danken. Sie waren immer für mich da, hatten ein offenes Ohr für mich und haben mich unterstützt wo sie nur konnten.

Contents

List of Figures

List of Tables

List of Abbreviations

ALOS	**A**dvanced **L**and **O**bservation **S**atellite
APRI	**A**ustrian **P**olar **R**esearch **I**nstitute
DEM	**D**igital **E**levation **M**odel
DInSAR	**D**fferential **SAR** **In**terferometry
DSAS	**D**igital **S**horeline **A**nalysis **S**ystem
EPR	**E**nd **P**oint **R**ate
ESA	**E**uropean **S**pace **A**gency
FB	**F**ine **B**eam
GRD	**G**round **R**ange **D**etected
HH	**H**orizontal–**H**orizontal
HS	**H**igh Resolution **S**taring Spotlight (TerraSAR-X)
HV	**H**orizontal–**V**ertical
IW	**I**nterferometric **W**ide swath mode
JAXA	**J**apanese **A**erospace E**X**ploration **A**gency
LOS	**L**ine **O**f **S**ight
NASA	**N**ational **A**eronautics and **S**pace **A**dministration
NSM	**N**et **S**horeline **M**ovement
ORFEO	**O**ptical **R**adar **Federated** **E**arth **O**bservation
PALSAR	**P**hased **A**rray **L**-band **S**ynthetic **A**perture **R**adar
PLR	**P**o**L**a**R**imetric
SAR	**S**ynthetic **A**perture **R**adar
SC	**Sc**anSAR
SLAR	**S**ide-**L**ooking **A**irborne **R**adar
SM	**S**trip**M**ap
SNAP	**S**enti**N**els **A**pplication **P**latform

SL	**S**ot**L**ight (TerraSAR-X)
SPT	**SP**o**T**light (PALSAR-2)
ST	**St**aring SpotLight
VH	**V**ertical–**H**orizontal
VV	**V**ertical–**V**ertical
WB	ScanSAR (PALSAR)
WD	ScanSAR (PALSAR-2)
WLR	**W**eighted **L**inear **R**egression
WS	**W**ide **S**wath mode

1. Introduction

1.1 Motivation

Arctic regions are one of the most rapidly changing environments on earth, and their coastlines are especially vulnerable to climate change (Lantuit, 2008, Overland et al., 2018). The annual erosion rates at the American and Canadian Arctic coastlines are among the highest in the world, but Siberian coastlines are also affected (Frederick et al., 2016). These irreversible coastal damages are a threat to communities and wildlife in those areas. Communities have needed to be relocated, and houses and archaeological sites have been damaged (Arp et al., 2010, Frederick et al., 2016, Jones et al., 2008, Radosavljevic et al., 2016). In addition to these directly visible effects, the erosion releases significant amounts of carbon dioxide (CO_2). The released CO_2 is absorbed by the ocean, which reduces its capacity to absorb atmospheric CO_2. This can cause a feedback loop that accelerates climate change and coastal erosion even more (Couture et al., 2018, Overland et al., 2018, Steele et al., 2008).

Arctic coastal erosion is often monitored through airborne and spaceborne optical imagery or in situ measurements (e.g. Cunliffe et al., 2019, Irrgang et al., 2018, Obu et al., 2016). In situ measurements only cover small areas, and optical images can be unreliable due to frequent cloud cover in the Arctic (Stettner et al., 2017, Zwieback et al., 2017). Unlike visible light, microwaves do not interact with clouds (Woodhouse, 2006). Their radiation is barely effected by the atmosphere, and does not rely on solar illumination, which can be especially useful for monitoring Arctic regions (Jones and Vaughan, 2010). This has motivated recent interest in using microwave technologies like Synthetic Aperture Radar (SAR) to monitor Arctic regions.

The interpretation of SAR data for coastal erosion in Arctic regions is a challenging research area (Stettner et al., 2017). Differential SAR interferometry (DInSAR) and SAR interferometry (InSAR) have been successfully used to measure gradual surface displacement in Arctic environments (Strozzi et al., 2018, Wang et al., 2017). However, detecting mass movements is difficult, because repeat-pass interferometry methods are

not effective in rapidly changing Arctic regions. The changes between the satellite revisit times are too large in comparison to the SAR wavelength, and no useful correlation can be found between the images (Zwieback et al., 2017). Therefore, Stettner et al. (2017) introduced a backscatter-based threshold method with TerraSAR-X images to classify and evaluate inter- and intra-annual cliff-top erosion rates. Unfortunately, only a limited number of high spatial resolution (in respect to the erosion rates) images of the Arctic region exist. This study tests this threshold-based method for lower-resolution PALSAR/PALSAR-2 L-band and Sentinel-1 C-band images in addition to high-resolution TerraSAR-X X-band images.

1.2 Objectives

The overall goal of this study is to advance SAR data analysis for coastal erosion measurements in rapidly changing Arctic environments. This is divided into two main objectives.

The first objective is to demonstrate threshold classification for X-band, C-band and L-band data. Specifically, the classification should correctly identify steep coasts, land, and water surfaces. To do this, the classification approach must quantify the dependence of backscatter on incidence angle, and then account for the angular dependence in the classification function. The classification should be applicable to various coast types, in various test areas and seasons, and for SAR data with various polarizations and spatial resolutions. The classification is tested with and without filtering to determine whether filtering improves the classification.

The second objective is to demonstrate the use of the classifications to analyze coastline movement in the Arctic. Specifically, seasonal and annual coastline movement rates should be calculated for steep cliff coastlines. Where steep cliff cannot be observed, e.g. in sandy environments or in SAR images in which the cliff faces away from the sensor, annual changes should be calculated using the boundary between areas classified as land and water. The accuracy of these estimates is assessed by comparison with optical images, previous studies, and cross-comparisons within this study.

2. Fundamentals

This chapter describes the relevant characteristics of Arctic coasts and Arctic coastal erosion processes in Section 2.1. Section 2.2 summarizes the main concepts of microwave remote sensing and the SAR technique (2.2.1), their measurement principles (2.2.2), and influences on the microwave backscatter that are important for the coastline detection procedure (2.2.3).

2.1 Arctic Coasts

One third of the world's coastlines are Arctic coasts (Lantuit, 2008). Arctic coastal banks are on average 8.4 m high, but backshore elevations vary regionally between 1.5 m to 14.5 m (Lantuit et al., 2012). All typical coastal features like beaches, barrier islands, deltas, salt marches, bluffs, and rocky cliffs can be found. The main differences between Arctic shorelines and shorelines in lower latitudes are the cold temperatures and the impact of snow and ice. The ice is often bound in permafrost. The evolution of coastal features occurs during thawing and sea-ice-free seasons (Kroon, 2014).

In general, Arctic coastal landscapes are classified as low-relief areas or high-relief areas. The main land-cover of low-relief Arctic coasts is tundra. Typically the coastal plains are flat, mildly sloped, and several hundreds kilometers wide, with no glaciers in the immediate surroundings. The morphology is shaped by thermokarst (e.g. ice wedges) and processes of the active layer on top of permafrost. The hinterland and tundra area is drained by large rivers, which create large offshore deltas (Kroon, 2014).

The main landscape features of high-relief coasts are glaciers, fluvial valleys, deltas, fjords, and open coastal water. Glaciers and land-ice masses are typically near the water. Glacial streams transport sediment, often forming alluvial fans or deltas (Kroon, 2014).

Like other coastal environments, Arctic coasts are influenced by the wind regime, the sediment-supply, and the oceanic and weather conditions of their climate (French, 2008).

Around 65% of Arctic coasts are unlithified and bonded only by permafrost (Irrgang et al., 2018). Arctic coastal plains can be stabilized by the ice, but they can also lose mass because of freeze–thaw cycles (solifluction) (Kroon, 2014). These conditions result in a process called thermal mechanical erosion: the combination of thermal abrasion caused by permafrost thawing and mechanical erosion caused by waves (Lantuit, 2008).

Waves erode the coastal base and carry away sediments, especially when sea ice is not present. During open-water (ice-free) periods, waves undercut the coastal bluff until the cliff collapses (Lantuit, 2008). Although nearshore sea ice causes a small amount of erosion by impacting the cliff, it mostly shields the cliff from the harsher impact of the waves (Barnhart et al., 2014). In some sheltered parts of the Canadian Arctic, the sea ice limits the open-water season to 8 to 10 weeks per year, while in areas like the Beaufort Sea and northern Siberia the open-water season lasts several months per year. In addition to seasonal variability of the sea ice extent, global warming is an important factor (French, 2008). Several studies show that the duration of the open-water season and the ocean surface and permafrost temperatures are increasing as the summertime sea-ice extent is decreasing (Barnhart et al., 2014, Hinzman et al., 2005, Romanovsky et al., 2010, Steele et al., 2008).

Depending on the morphology of the coastline and the ground ice content, thermoabrasion (block failures) or thermodenudation (retrogressive thaw slumps) cause erosion (Hoque and Pollard, 2009, Lantuit, 2008). Coastal zones with horizontal thermo-erosional niches, especially when combined with large surface areas separated by ice wedges, are prone to block failures (Hoque and Pollard, 2004). Refer to the schematic in Fig. 2.1. The thermal-mechanical erosion undercuts the frozen cliff, and under the weight of gravity a large block of soil detaches from the coast (Lantuit, 2008).

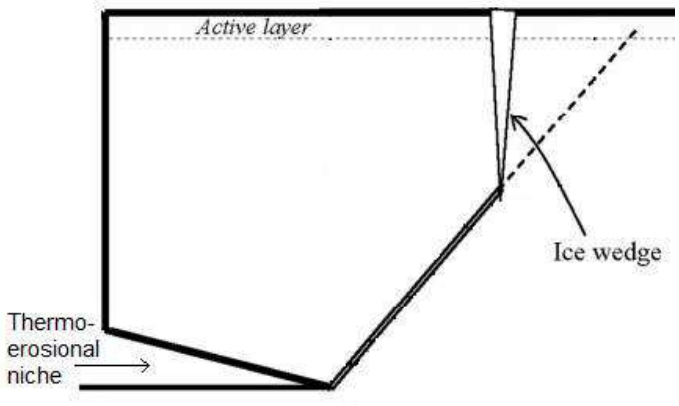

FIGURE 2.1: Schematic of vertical cliff with horizontal thermo-erosional niche and ice wedge, adapted from: Hoque and Pollard (2004)

Retrogressive thaw slumps occur where ice-rich permafrost is exposed to thaw, and they are one of the most rapid erosion processes in the arctic. Thaw slumps develop when slopes are undercut by wave or stream action and the soil collapses (French, 2008, Zwieback et al., 2017). This process typically consists of three main features: a c-shaped 1–2 m tall headwall, a 20 to 50° angled headscarp, and a slump floor (scar zone). These features are sketched in Fig. 2.2. Most of the active layer and ice-poor organic or inorganic materials are present in the headwall. The headscarp retreats because of the ablation of the ice-rich materials. During this process, sediments and meltwater are released and accumulate at the slump floor (Lantuit and Pollard, 2008). Active thaw slumps can grow uphill several meters per year, but most of them are stabilized within 30–50 summers (French, 2008, Zwieback et al., 2017). However, erosion processes in the slump floor can trigger a new retrogressive thaw slump within an existing or stabilized one, leading to polycyclic slumps (Lantuit and Pollard, 2008).

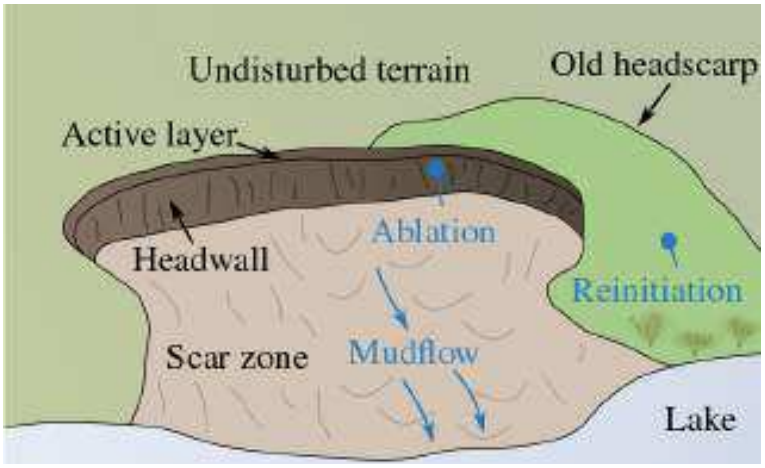

FIGURE 2.2: Schematic of a thaw slump. Processes are illustrated in blue and features in black, source: Zwieback et al. (2017)

On average the erosion rate on Arctic coasts is 0.5 m/year, but in the Lapev East Siberian and the US and Canadian Beaufort Seas the rates are even higher (3 m/year). Figure 2.3 shows the coastal change rates of an 101,447 km Arctic coastline segment.

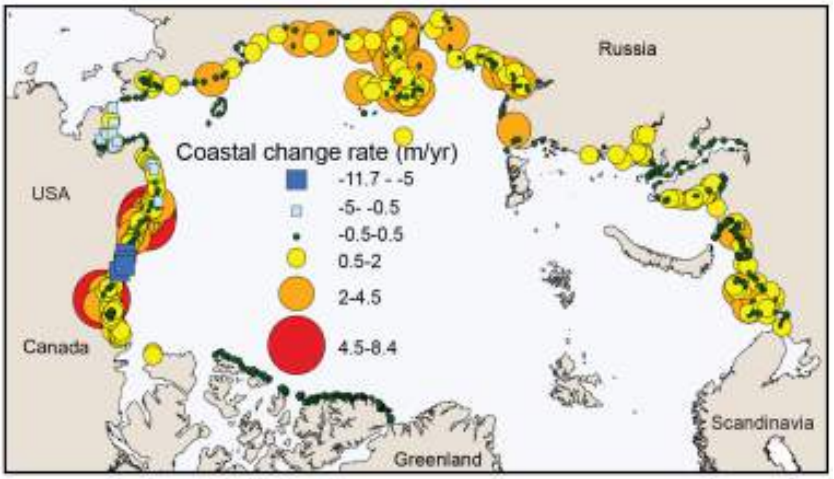

FIGURE 2.3: Overview of the Arctic coastal erosion rates. Negative values indicate erosion, source: Barnhart et al. (2014)

2.2 Microwave Remote Sensing

Microwaves are in the non-optical region of the electromagnetic spectrum, with wavelength around 1 mm up to 1 m, equal to frequencies between 0.3 to 300 GHz (Albertz, 2009, Woodhouse, 2006). However, the exact boundaries defining the wavelength of the microwave region are ambiguous (Woodhouse, 2006). The electromagnetic spectrum from the ultraviolet to the microwave spectrum can be seen in Fig. 2.4. For Remote Sensing different microwave bands are used, and the use of letters to categorize the different bands is widespread. The bands used in this study are listed in Table 2.1. Similar to the definition of the microwave range, slightly different boundaries of the bands can be found in literature (Albertz, 2009, Jones and Vaughan, 2010).

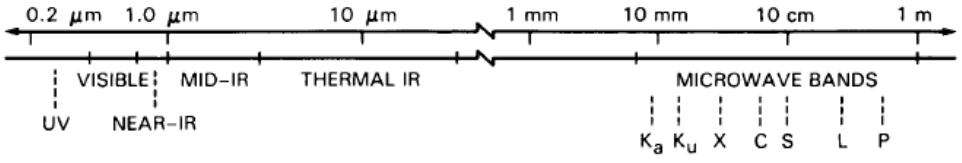

FIGURE 2.4: Electromagnetic spectrum, source: NASA (1989)

Bands	Frequency [GHz]	Wavelength [cm]
X	7-12	2.4-4.5
C	4-7	4.5-7.5
L	1-2	15-30

TABLE 2.1: Microwave bands that are relevant for this study, data source: Albertz (2009)

In general, microwave remote sensing instruments can be divided into two categories: passive and active. Passive instruments, called radiometers, measure microwaves that are radiated or reflected by the target (Albertz, 2009, Woodhouse, 2006). Active instruments, also known as radars, are based on the principle of echolocation. They generate a signal (usually wavelengths between 1 and 100 cm), send it to the target, and measure the signal scattered back.

The active systems can further be divided in non-imaging systems like altimeters and scatterometers and imaging systems like Side-Looking Aperture Radar (SLAR) and Synthetic Aperture Radar (SAR). Altimeters make very precise distance measurements, and scatterometers accurately characterize the backscatter properties of the target with a low spatial resolution. Imaging radars create maps of microwave backscatter, which look similar to black-and-white optical images (Woodhouse, 2006). SLAR and SAR produce medium- and high-resolution backscatter images. This study uses SAR data, which is described below.

2.2.1 Synthetic Aperture Radar

The Synthetic Aperture Radar is an improvement of the SLAR technique, and makes it possible to produce high-resolution images in the range of meters to hundreds of meters (Albertz, 2009, Woodhouse, 2006).

The SLAR antenna emits microwaves to observe a target area obliquely to the side of the aircraft. Diffraction causes the beam of the emitted microwaves to spread out in a cone. The semi-angle of this cone, θ, depends on the wavelength, λ, and the diameter of the antenna, d. For small θ, the diameter of the observed footprint can be approximated by θ and the height of the platform above the surface, H, as: $H\theta$ or $H\frac{\lambda}{d}$ (Jones and Vaughan, 2010). Therefore, the spatial resolution in flight-line direction (azimuth resolution) can only be improved by a shorter wavelength or a larger antenna. However, the frequency domain of the microwave region is small, and the physical size of a spaceborne antenna is limited to about 10 m.

To improve upon the limited resolution of SLAR imaging, SAR instruments use a small moving antenna to synthesize a much larger antenna. The antenna is designed to have a very wide beam, so that adjacent observing footprints overlap (Jones and Vaughan, 2010, Woodhouse, 2006).

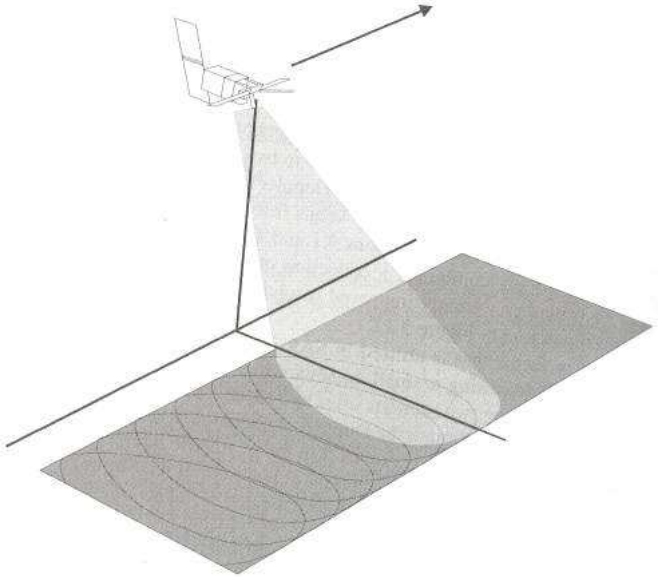

FIGURE 2.5: SAR sensing geometry, source: Woodhouse (2006)

The continuously moving SAR platform makes very precise measurements of the frequency of the returned signals and analyzes the signal's Doppler shift to calculate the origins of each echo. Echos coming from the back part of the beam are Doppler-shifted to lower frequencies and echos from the front are shifted to higher frequencies. The Doppler frequency, f_D, is given by (Woodhouse, 2006):

$$f_D = 2\frac{V_{rel}}{\lambda} \tag{2.1}$$

where V_{rel} is the relative velocity between the sensor and the target. The relative velocity V_{rel} can be calculated as a function of the angle between the target and the beam center, θ_a, (Woodhouse, 2006):

$$V_{rel} = V_s sin\theta_a \tag{2.2}$$

where V_s is the speed of the platform. The domain of θ_a is defined by the half beamwidth of the antenna, so f_D has its maximum and minimum when the target enters and leaves the beam, respectively. When θ_a is small, $\sin\theta_a \approx \theta_a$, which leads to (Woodhouse, 2006):

$$sin\theta_a \approx \theta_a = \frac{\lambda}{2D}. \tag{2.3}$$

The shortest temporal distance between signals that the sensor can differentiate, p_t, can be calculated with the Doppler bandwidth, B_D (Woodhouse, 2006):

$$p_t = \frac{1}{2f_D} = \frac{1}{B_D}. \tag{2.4}$$

To determine the azimuthal resolution, it is necessary to include the speed of the platform, V_s, into the equation (Woodhouse, 2006):

$$p_a = \frac{V_s}{B_D} = \frac{V_s \lambda 2D}{4V_s \lambda} = \frac{D}{2}. \tag{2.5}$$

Small antennas have a larger beam-width, which causes a much larger range of V_{rel} and Doppler-bandwidth. Therefore the azimuth spatial resolution improves as antenna length decreases and is independent of the wavelength and sensor–target distance. Nevertheless, due to compromises that come with a smaller antenna like weaker signal strength, the azimuth resolution of SAR sensors is limited. Furthermore, the theoretical resolution of $\frac{D}{2}$ cannot be fully achieved in practice (Woodhouse, 2006).

2.2.2 Measurement Principles of Active Sensors

Active microwave sensors are based on the principle of echolocation. They transmit a signal, and measure the returning echo that was scattered by the target. The radar equation estimates what fraction of the transmitted signal is returned from the target (Woodhouse, 2006):

$$P_s = \frac{P_t G^2 \lambda^2 \sigma}{(4\pi)^3 R^4} \tag{2.6}$$

P_t is the power emitted from the antenna, P_s is the power entering the receiving antenna, R is the distance to the target, and G^2 characterizes the directivity and electrical efficiency of both the transmitter and receiver. The effective area of the receiver is given by $\frac{G\lambda^2}{4\pi}$, and the spreading loss on the way to the target and back is characterized by $\frac{1}{(4\pi)^2 R^4}$ (Woodhouse, 2006). The backscattering cross-section σ accounts for various properties of the target that are discussed in Section 2.2.3.

In remote sensing the area-normalized cross-section, σ_0, is commonly used instead of σ when the observed targets are an area instead of a specific object. For a target of area

A, σ_0 is defined (Woodhouse, 2006):

$$\sigma_0 = \frac{\sigma}{A}. \tag{2.7}$$

The normalized radar cross-section is independent from the footprint or spatial resolution of a sensor and is therefore a characteristic property of the observed target area (Woodhouse, 2006). In many studies σ_0 is expressed in decibels as (e.g. Antonova et al., 2016, Stettner et al., 2017):

$$\sigma_0[dB] = 10 \log 10(\sigma_0). \tag{2.8}$$

2.2.3 Backscatter Influences

For analyses with SAR data, it is important to understand the mechanisms creating the microwave backscatter. For natural surfaces σ_0 is mainly influenced by the imaging geometry, the reflectivity of the surface, and its roughness in comparison to the wavelength (Woodhouse, 2006).

Imaging Geometry

The side-looking geometry of the SAR antenna causes geometric distortions in the image that vary as a function of the slope of the surface and the incidence angle. The antenna receives echo signals from high-altitude features comparatively faster than from low features, which distorts the measured distances. Slopes facing the sensor are projected narrower and appear brighter than identically shaped slopes facing away from the sensor. The geometric distortion can be corrected with an orthorectification of the image.

The extreme case of this foreshortening effect is called layover. Here, the top of the highest object is closer to the antenna than the object at the nadir (directly below the satellite). In the image the highest object would than appear to lean over into the direction of the sensor.

Surfaces that lie behind other objects are affected by the shadowing effect. From these hidden regions no signal returns to the sensor. In contrast to the foreshortening effect, the shadow effect gets worse the further the region is away from nadir. Radar shadow generally appears at local incidence angle greater than 90°, i.e. the surface is facing away from the instrument (Woodhouse, 2006).

The foreshortening effect is especially important for this study. It can be used to map steep arctic coasts that face the instrument. The microwave backscatter of these areas is high in comparison to water or other land areas, so high resolution X-Band images can identify the steep coasts (Stettner et al., 2017).

Surface Roughness and Incidence Angle

The roughness of a material is the main factor determining whether the beam specularly reflects or scatters (Jones and Vaughan, 2010). Here roughness is defined with respect to the microwave wavelength, which ranges from 2.4 to 30 cm for the bands analyzed in this study. A smooth surface reflects the entire beam in a single direction. Unless the surface happens to be facing the sensor, nearly no signal returns to the sensor, and the surface appears dark on the image. However with rough surfaces the microwave is diffusely scattered by the surface, and a larger portion of the signal returns to the sensor (Albertz, 2009). A special case is the double-bounce effect, which takes place when two orthogonal, highly reflective surfaces cause high backscatter values. Examples for this effect can be seen in Fig. 2.6.

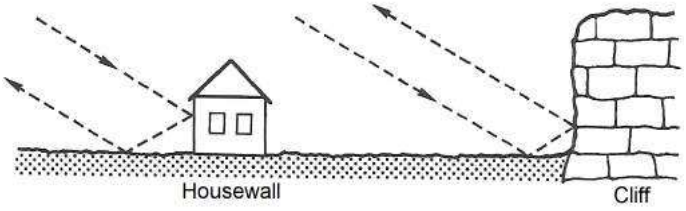

FIGURE 2.6: Two examples of the double-bounce effect, source: Albertz (2009)

In addition to roughness, the angle of illumination also has to be taken into account. Except for extremely rough surfaces, the scattering field is defined by the surface roughness and the incidence angle of the microwave as illustrated in Fig. 2.7. Therefore, especially for slightly rough surfaces, the total amount of scattered energy depends on both the surface roughness and the incidence angle. Active microwave sensors observe at very high incidence angles, which makes them subject to these effects (Woodhouse, 2006). Classification approaches for large study areas that analyze SAR images from multiple incidence angles need to account for the dependence of σ_0 on incidence angle (e.g. Bartsch et al., 2017).

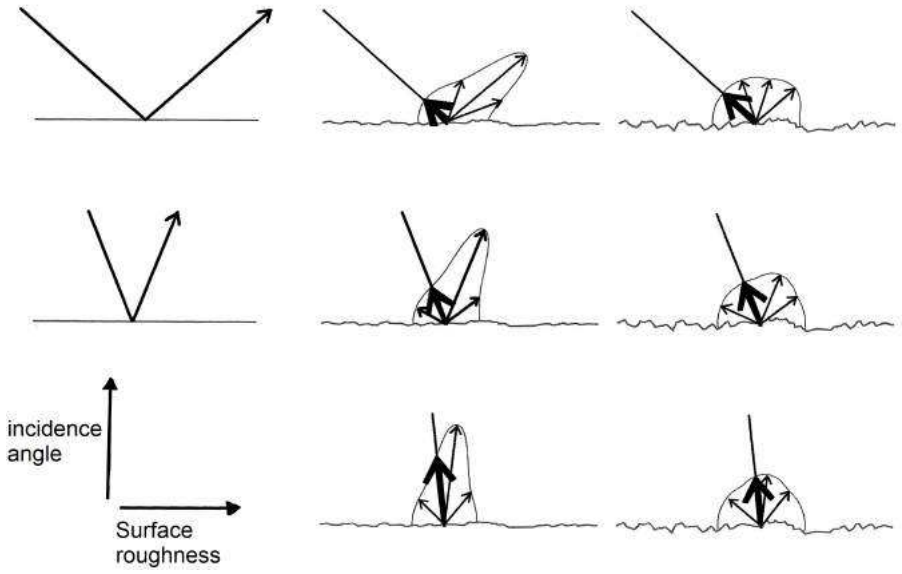

FIGURE 2.7: Effect of incidence angle and surface roughness on σ_0. From left to right: smooth, medium rough, and rough surface, source: Woodhouse (2006)

Polarization

Active microwave remote sensors can send and receive microwaves that are polarized in only one direction. For example, they can send microwaves linear horizontal to the ground (H) or linear vertical to the ground (V). The received signal can also either be horizontal or vertical. This results in four different types of polarized waves: HH, HV, VH and VV as shown in Fig. 2.8. Depending on their polarization, microwaves interact differently with the surface. Effectively, objects have different σ_0 for HH, HV, VH, and VV waves. This can be used to detect different features on the surface. Forest studies for example, use the HH waves to observe the ground of the forest, while VV waves are used to see the reflection of the trunks of the trees, and the HV/VH waves can be used to analyze the reflections of the branches and leaves (JAXA, 2018).

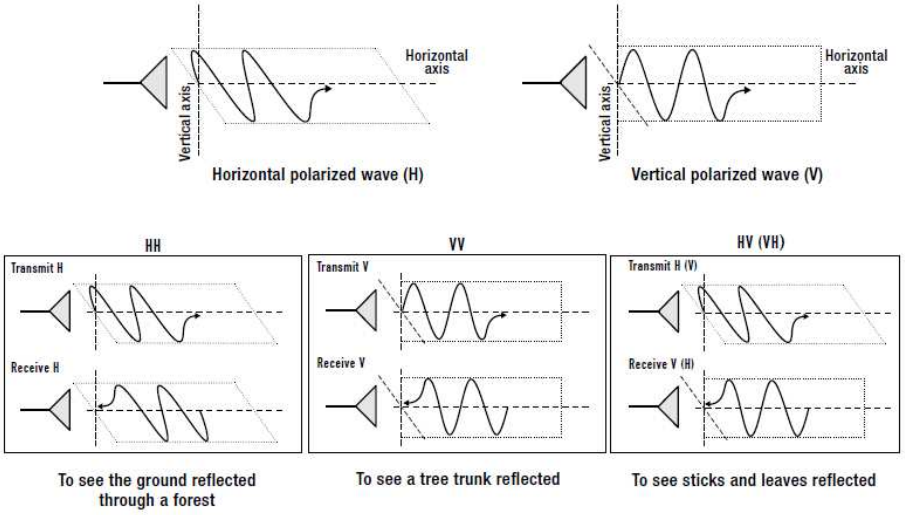

FIGURE 2.8: Polarizations of electromagnetic waves and their use for forest monitoring. Source: JAXA (2018)

Coastline mapping studies indicate that SAR images with large incidence angles ($> 30°$) show a high-contrast water–land boundary, regardless of polarization. In co-polarized images (HH or VV) with lower incidence angles, the contrast between water and land is often poor, which makes a land–water classification difficult, particularly in windy conditions. (Wind increases the roughness of the water.) At lower incidence angles, cross-polarized images (HV or VH) tend to show higher land–water contrast, improving classification results (Baghdadi et al., 2007).

Dielectric Properties and Wavelength

The dielectric properties of the observed surface have a significant influence on the microwave interaction. Metallic surfaces or surfaces with high dielectric constants, like wet soils, efficiently reflect the microwave signal, and the waves cannot penetrate deep into the surface. On the other hand, surfaces with a low dielectric constant, like dry snow, have a lower reflectivity, and the penetration depth is higher (Albertz, 2009).

The wavelength is another factor that determines the penetration depth into the surface material. Long microwaves penetrate relatively deep into materials with low dielectric constants. The penetration depth of short wavelengths is much lower. This causes σ_0 to vary as a function of wavelength (Woodhouse, 2006). Figure 2.9 shows this relationship.

In general, L-Band data seems to provide good contrast for classifying different types of bare ground in Arctic areas, while X- and C-Band data are better to characterize wetland vegetation (Ullmann et al., 2017). The backscatter at steep Arctic coasts is

high because of foreshortening, and it is even higher in summer. The summer increase indicates that the change in the dielectric properties of the surface (more soil moisture) increases the backscatter at these coast areas in addition to the foreshortening (Stettner et al., 2017).

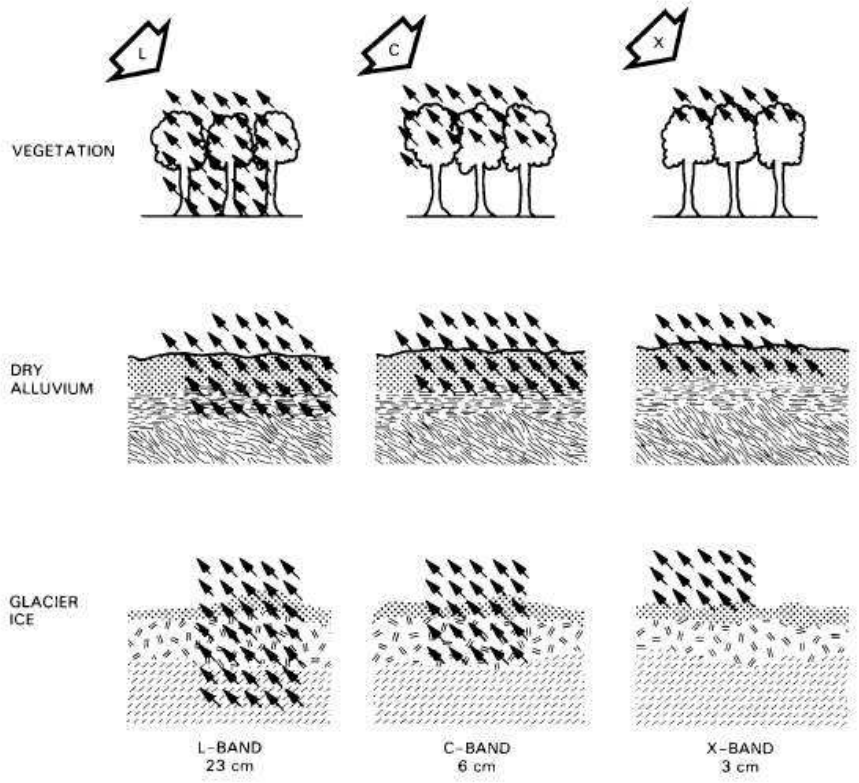

FIGURE 2.9: Relationship between penetration depth, dielectric properties, and the observation wavelength. Three different surface examples are displayed: vegetation, dry alluvium and glacier ice, source: NASA (1989)

3. Data Description

In this chapter, Section 3.1 gives an overview of the study areas. The used SAR sensor types and satellites are described in Section 3.2.

In addition to SAR data, various optical and classification data was used in this study, for example to visually assess the calculated classifications. A short description of this auxiliary data is given in Section 3.3.

3.1 Areas of interest

This study focuses on low-relief coasts in three main areas: the Canadian Yukon Coast, the Russian Bykovsky Peninsula and Barents Sea Coast. These areas are marked in Fig. 3.1.

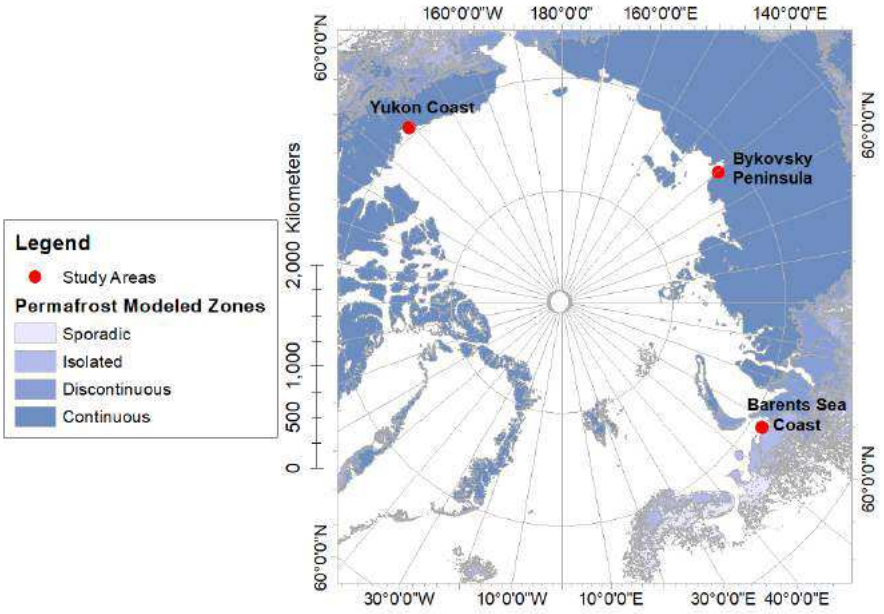

FIGURE 3.1: The three study areas in the arctic and their modeled permafrost zones, data source: Obu et al. (2018)

3.1.1 Yukon Coast

The approximately 280 km long Yukon Coast lies between the Alaskan border and the Mackenzie Delta in Canada (Fig. 3.2). The climate has a continental character in winter and maritime influences in summer. Komakuk Beach, around 40 km west from Herschel Island, is the closest weather station in this area (Obu et al., 2016). From 1971 to 2000 the mean air temperature was −11°C. The coldest temperatures were measured in February and the warmest in July, with averages of −25.3°C and 7.8°C (Government Canada, 2019). The coastal areas of the Beaufort Sea are typically ice-covered from October to June. From late August to September, storm winds become increasingly frequent and can generate significant high waves greater than 4 m (Solomon, 2005). The coastal erosion processes manly take place during this ice-free storm season (Obu et al., 2016).

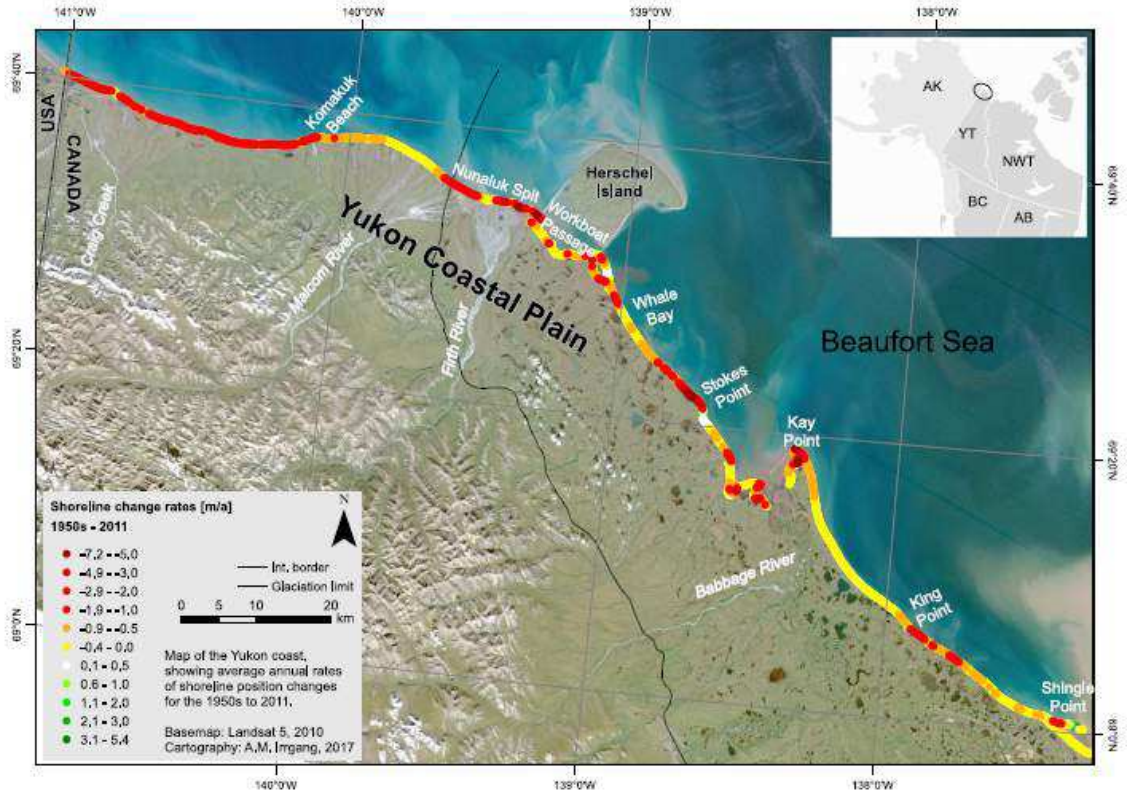

FIGURE 3.2: Calculated erosion rates from 1950–2011 for the Yukon coast. Rates < 0 indicate erosion, source: Irrgang et al. (2018)

In this area, low-relief landforms like coasts, beaches, barrier islands and spits, inundated tundra, tundra flats and slopes, and active cliffs are common (Irrgang et al., 2018). Around 33% of the coast is active slumps, and 13% is high bluffs with no slumping. These landforms exist for example on Herschel Island. Beach-protected coast parts like

the area around Stokes Point comprise 12% of the total coastline. Stabilized slumps and low bluff coasts are also present in that area and make up 19% and 23% of the total shoreline, respectively (Obu et al., 2016).

In 2006 around 78% of the coastline, including Herschel Island, was affected by coastal erosion processes (Obu et al., 2016). Excluding Herschel Island, the mean annual rate of shoreline change from 1950 to 2011 was $-0.7\pm$ 0.2 m/year. The highest erosion rates, $-7.2\pm$ 0.2 and $-6.2\pm$ 0.2 m/year, were measured at Nunaluk Spilt and Stokes Point (Fig. 3.2). Beaches, barrier islands, and spits are the main landform at these two sites (Irrgang et al., 2018).

3.1.2 Bykovsky Peninsula

The Bykovsky peninsula is located north-east of Tiksi in Russia (Fig. 3.3), and lies within the zone of continuous permafrost. The weather has an almost continental character, although it is surrounded by the Laptev sea (Lantuit et al., 2011). The mean annual temperature is $-11.5°C$, with long harsh winters and short cold summers. The open water season is between July and September, but can begin as early as late May (Günther et al., 2013, Lantuit et al., 2011). Concurrent with the open water season, the highest storm activities take place in these months (Lantuit et al., 2011). Storms are the largest driver of erosion, and therefore the coastal erosion is mostly limited to the open water season in July to September. However, even during this time chunks of sea ice can reduce the wave activity (Lantuit, 2008).

The relief of the peninsula is dominated by flat elevated areas up to 40 m above sea level and thermocarst depressions near sea level (Grosse et al., 2005). At the over 150 km long shoreline, various coastal landforms exist, such as sandbars, lagoon barriers, ice complex cliffs, thermokarst basins (alases), and thaw slump coasts (Fig. 3.3). Between 1951 and 2006, alases and retrogressive thaw slumps underwent erosion at a rate of 1.02 and 0.91 m/year, respectively. These rates are significantly higher than the other coast types, which underwent erosion at rates between 0.40 and 0.47 m/year (Lantuit et al., 2011).

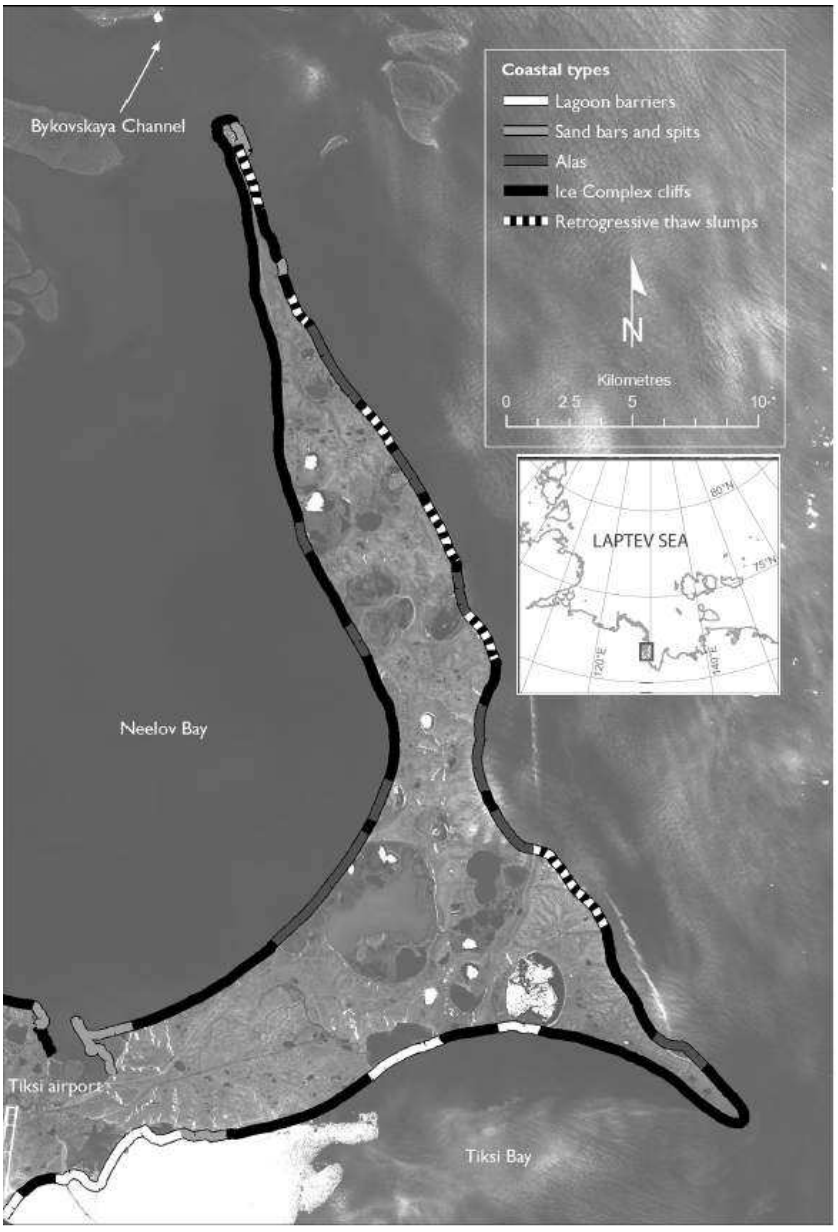

FIGURE 3.3: Coast types of the Bykovsky Peninsula, source: Lantuit et al. (2011)

3.1.3 Barents Sea Coast

The study region at the Barents sea coast in the northwest of Russia lies in the zone of continuous permafrost (Fig. 3.4), but is warmer than the other sites. The mean annual air temperature in 2012–2014 was between −3.8 and −4.8°C. The coldest air temperature of −39.4°C was measured in January, and the warmest, 30°C, in July (Le et al., 2018). Storm surges with magnitudes of 1.5 m to 2 m, and tides with high amplitudes of 0.5 m are common (Leont'yev, 2003).

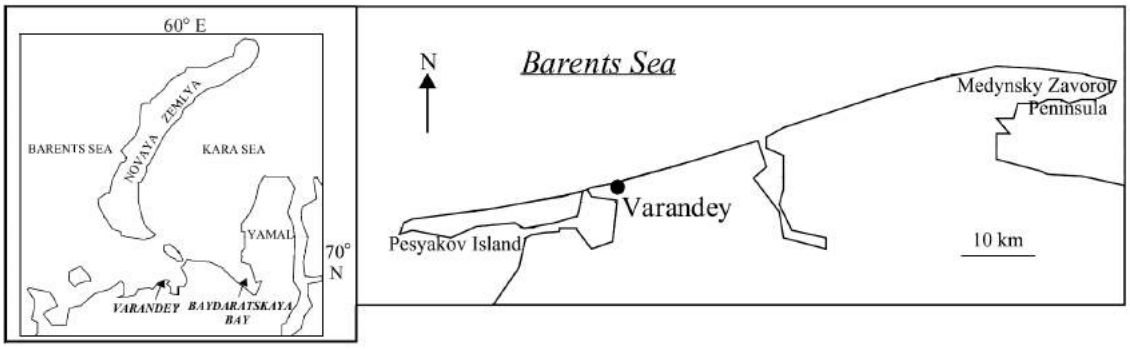

FIGURE 3.4: Location of the Barents Sea coast, adapted from source: Barnhart et al. (2014)

In general, the landscape varies from wide, low-gradient sandy shores with dune belts to sub-vertical ice-rich bluffs and narrow beaches (Guégan et al., 2016). The coast is formed by a marine terrace 2 to 6 km wide, and the sediment body is predominantly sand. The coastal cliffs are mostly between 3 m and 10 m high. Thermal erosion only locally occurs, and does not play a large role in the coastal dynamics. Coastal erosion rates of 1 to 4 m/year are common (Leont'yev, 2003).

3.2 SAR Data

The used PALSAR/PALSAR-2 and Sentinel-1 data sets in this study were recorded in the most likely open water months, from June to September. This time frame was chosen to take advantage of the backscatter difference between land and water, which is greater than the difference between land and sea ice. The PALSAR and PALSAR-2 data sets cover the longest time span (2007, 2008, 2017, 2018). Comparable Sentinel-1 data was available for the years 2017 and 2018. The high-resolution TerraSAR-X data sets were available for June, July, August and October 2018 and January 2019. Table 3.1 summarizes the used images. It is important to mention that, although all compared images have the same orbit path, slightly different orbit variations can occur.

Sensor	Region	Date	Resolution [m]	Pass Designation
PALSAR/ PALSAR-2 (HH, HV)	Yukon Coast (West)	2007-08-31	20	Ascending
		2008-09-02	20	Ascending
		2017-07-26	10	Ascending
		2018-07-25	10	Ascending
	Yukon Coast (East)	2007-08-31	20	Ascending
		2008-09-02	20	Ascending
		2017-06-19	10	Ascending
		2018-07-30	10	Ascending
	Bykovsky Peninsula	2007-09-04	20	Ascending
		2008-09-06	20	Ascending
		2017-09-05	10	Ascending
		2018-07-08	10	Ascending
	Barents Sea Coast	2007-08-01	20	Ascending
		2008-08-03	20	Ascending
		2017-09-03	10	Ascending
		2018-07-14	10	Ascending
Sentinel-1 (VV, VH)	Yukon Coast (West)	2017-07-15	20	Ascending
		2018-07-22	20	Ascending
		2017-07-29	20	Descending
	Yukon Coast (East)	2017-07-17	20	Ascending
		2018-07-24	20	Ascending
	Bykovsky Peninsula	2017-07-25	20	Descending
		2018-07-20	20	Descending
	Barents Sea Coast	2017-07-28	20	Descending
		2018-07-23	20	Descending
TerraSAR-X (HH)	Yukon Coast (East)	2018-06-15	0.62	Descending
		2018-07-07	0.62	Descending
		2018-07-18	0.62	Descending
		2018-07-29	0.62	Descending
		2018-07-13	0.69	Ascending
		2019-01-27	0.69	Ascending
		2018-07-16	0.96	Descending
		2018-10-12	0.96	Descending
		2018-08-12	1.35	Descending

TABLE 3.1: List of the used images grouped by sensor.

3.2.1 PALSAR and PALSAR-2

The Phased Array type L-band Synthetic Aperture Radar (PALSAR) and PALSAR-2 are Japanese L-band SARs with a center frequency around 1.2 GHz (JAXA, 2008, 2018). PALSAR was launched on board the Advanced Land Observation Satellite (ALOS) in January 2006 and sent information until its failure in April 2011. ALOS was replaced in May 2014 by ALOS-2, carrying the PALSAR-2. Both satellites have a sun-synchronous, sub-recurrent orbit, but the 14-day revisit time of ALOS-2 is much shorter than the ALOS revisit time of 46 days (JAXA, 2018, Shimada, 2009). Due to their duration and orbits, the PALSAR datasets are good for long-term studies of the Arctic.

The senors can be used in different observation modes with variable polarization, incident angle, swath width and spatial resolution (Table 3.2 and Fig. 3.5). In general PALSAR has three different modes: the Fine Beam (FB), ScanSAR (WB) and Polarimetric (PLR). The FB mode can further be divided in a single polarization mode (HH), a dual polarization mode (HH and HV) or a polarimetric mode (HH, HV, VH and VV) with spatial resolutions of 10 m, 20 m, or 30 m, respectively.

Sensor Mode	Polarization	Off-nadir Angle	Pass Designation	Coverage	Time Window	Observation Frequency	Spatial Resolution
Fine Beam single pol.	HH	34.3°	Ascending	Global	Dec-Feb	1-2 obs/year	10 m
Fine Beam dual pol.	HH+HV	34.3°	Ascending	Global	May-Sep	1-4 obs/year	20 m
Fine Beam polarimetric	HH+HV+ VH+VV	21.5°	Ascending	Regional	March-May	2 obs/2 year	30 m
ScanSAR	HH	20.1°-36.5°	Descending	a)Global b)Regional	Jan-Dec	a)1 obs/year b)8 obs/year	100 m

TABLE 3.2: PALSAR acquisition modes, source: ESA (2007)

Like PALSAR, the PALSAR-2 sensor has three observing modes: the Spotlight (SPT) mode, the Stripmap (SM) mode, and the ScanSAR (WD) mode (Fig. 3.5). The SPT mode, with a swath width of 25 km x 25 km, enables increased illumination time with electronic azimuthal beam steering, which results in images with a high resolution of 1×3 m. The SM mode has a relatively wide swath width of 50–70 km with a good spatial resolution of 3 m (SM1), 6 m (SM2) or 10 m (SM3). The lowest image resolution of 60 m (WD2) or 100 m (WD1) with an extremely wide observation footprint (swath widths of 350–490 km) are achieved with the WD mode. The resulting resolution of the SM and WD modes are comparable to the FB and WB modes of the PALSAR sensor. The Spotlight mode however, was not available with PALSAR (JAXA, 2018).

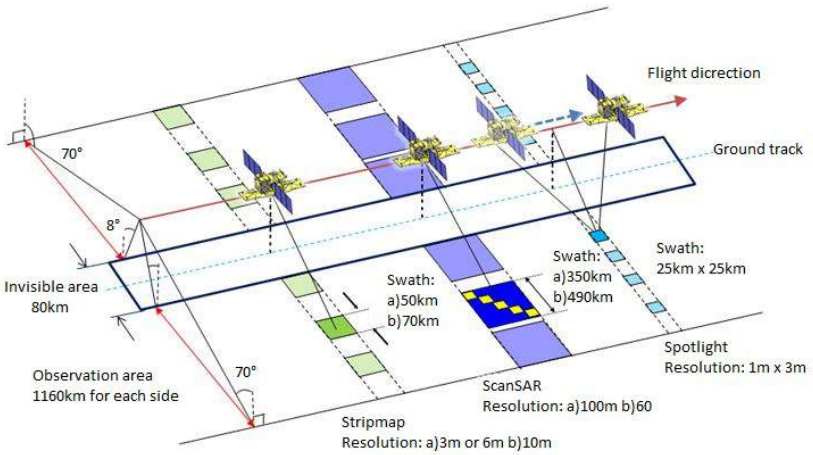

FIGURE 3.5: PALSAR-2 acquisition modes, source: JAXA (2018)

Two sets of data were used from the PALSAR satellites. First, PALSAR FB dual polarization images with 20 m resolution in HH and HV polarizations were analyzed. Second, PALSAR-2 SM3 images with 10 m resolution, also in HH and HV polarizations, were analyzed. In total four images with the same orbit, one image per year, for each area of interest were analyzed.

3.2.2 Sentinel-1

The Sentinel-1 mission is part of ESA's Copernicus program. The mission contains two satellites with a near-polar, sun-synchronous orbit, 180 degrees apart from each other. The two earth observation satellites Sentinel-1A (launched in April 2014) and Sentinel-1B (launched in April 2016) have an identical C-band SAR sensor on board (Schubert et al., 2017). The sensors can be used in four different operation modes: the Interferometric wide-swath mode (IW), the Wave mode (WV), the Strip Map mode (SM) and the Extra wide-swath mode (EW) (Fig. 3.6).

The IW mode combines a wide swath width of 250 km with a relatively good ground resolution of 5×20 m. The incidence angle range is 31° to 46°. Images can be captured in dual polarization (HH+HV or VV+VH).

The WV data is composed of single strip map operations with an alternating elevation beam in a mid-incidence angle range of 23° to 37° and a fixed on/off cycle. This results in 20×20 km vignettes in 100 km intervals. The WV is just available in single polarization (HH, VV).

The SM mode provides data with a high ground resolution of 5×5 m, but a smaller swath width of 80 km. It operates at incidence angles between 20° and 47°, with dual polarization.

The widest swath (400 km) is achieved in the EW mode. It has the same incidence angle range and polarization modes as the SM mode, and generates images with a medium ground resolution of 20×40 m.

For the IW and EW mode the TOPSAR technique is used. In this technique the beam is not just steered in range like with ScanSAR, but also electronically steered back-to-front in the azimuth direction within each burst (ESA, 2012).

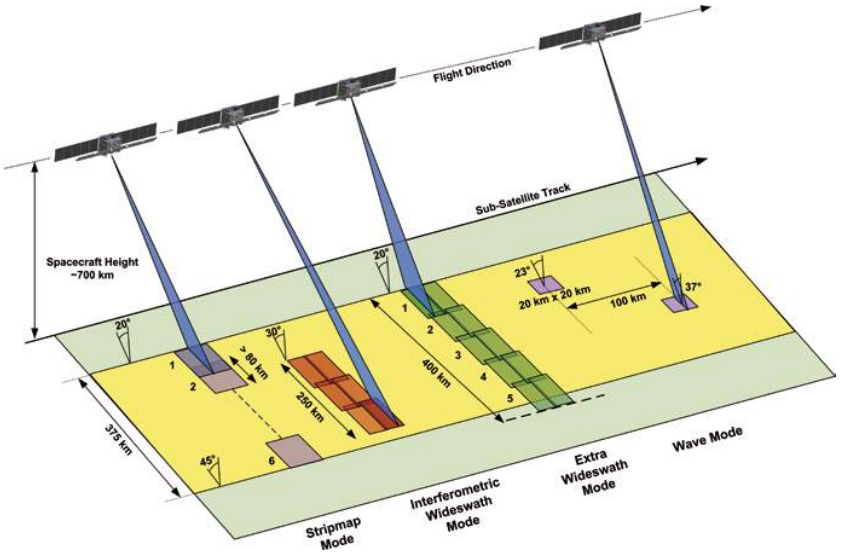

FIGURE 3.6: Sentinel-1 acquisition modes, source: ESA (2012)

For this study Sentinel-1 IW images with a ground resolution of 20 m were used. Like the PALSAR/PALSAR-2 data sets, one image per year with the same orbit for every area of interest was analyzed. The years 2017 and 2018 were chosen to make a result comparison of the coastal erosion rates with the PALSAR/PALSAR-2 images possible. Images with ascending and descending pass directions were available for the Yukon Coast, and both were used for this study.

3.2.3 TerraSAR-X

TerraSAR-X was launched in June 2007, and is a commercial German X-band SAR earth observation satellite. It has a sun-synchronous orbit and a repeat period of 11 days. The standard operational mode is the single receive antenna mode, which can be used in three different modes: SpotLight (SL), StripMap (SM) and ScanSAR (SC).

The SpotLight mode uses phased array beam steering in azimuth direction to increase the illumination time. It can further be divided in the High Resolution SpotLight (HS) and Staring SpotLight(ST) mode. HS has a azimuth resolution of 1.1 m and a standard scene size of 10×5 km. Dual (VV and HH) or single (VV or HH) polarizations are available for SL and HS. The ST scene size is highly dependent on the incidence angle, because the antenna footprints depends on the scene, and the scene length corresponds to the length of the antenna footprint. The Spotlight mode achieves an azimuth resolution up to 0.24 m. For this mode only single polarization images are available.

In SM mode the antenna beam is fixed in elevation and azimuth, and the ground swath is illuminated with a continuous sequences of pulses. This results in a spatial resolution up to 3 m and a standard scene size of 30×50 km.

TerraSAR-X has two ScanSAR modes: the basic ScanSAR (SC) and the Wide ScanSAR (WS) mode. The ScanSAR mode creates slightly overlapping footprints with different incidence angles, and processes them into one scene. With this technique, swath widths of 100 km or more and a spatial resolution of 18.5 m can be achieved. Swath width up to 270 km and a spatial resolution of 40 m are possible in WS mode (Airbus, 2015).

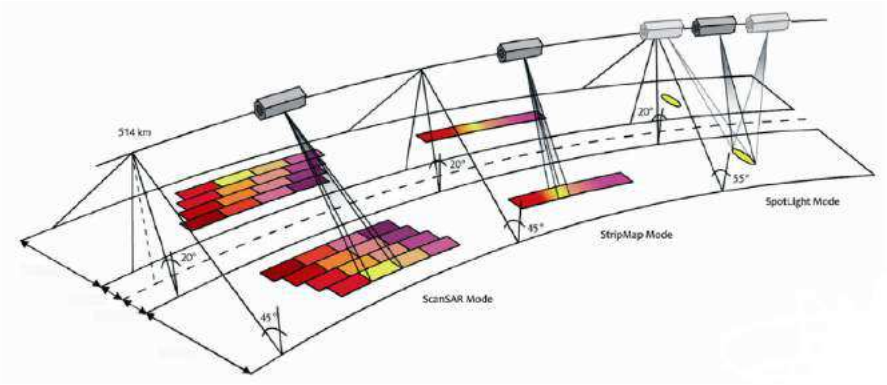

FIGURE 3.7: TerraSAR-X acquisition modes, source: Airbus (2015)

In this study TerraSAR-X images in ST mode with a HH polarization and incidence angles between 19° and 51° were used. Nearly all images have an ascending pass designation and cover areas at the Yukon Coast.

3.3 Auxiliary Data

Sentinel-2, Landsat 7/8, Péiades, and Google Earth optical images were used in this study to visually assess the classification results. In addition, landcover classifications provided by (Bartsch et al., 2019) were used to calculate the coastline orientation.

Sentinel-2 is an European mission to deploy wide-swath, high-resolution, multi-spectral observation satellites. It deployed two twin satellites, Sentinel-2A and -2B, in a sun-synchronous orbit 180° apart from each other. Sentinel-2A was launched in June 2015 and Sentinel-2B in March 2017. The optical sensor samples 13 spectral bands. The spatial resolution depends on the used band: four bands have a spatial resolution of 10 m, six bands of 20 m, and three bands of 60 m (ESA, 2015). This study uses Sentinel-2 true color images (band 4, 3 and 2) with a spatial resolution of 10 m. The images were acquired in the summer months of 2017 and 2018.

NASA's Landsat mission deployed a series of land observation satellites. The first satellite was launched in July 1972. Landsat 7 was launched in April 1999, and provides visible-, infrared-, and thermal-wavelength images of all land and near-coast areas on Earth. It has eight different bands with resolutions between 15 m and 30 m. A scan-line-corrector failure in 2003 destroyed the instruments ability to compensate for the forward motion of the satellite. The edges of the images now contain alternating scan lines of missing data (USGS, 2018). Landsat 8 was launched in February 2013, and operates in the visible, near-infrared, short wave infrared, and thermal infrared regions. It has eight bands with a spatial resolution of 30 m and a unique 15 m Pan band (USGS, 2019). This study used Landsat 7 images acquired in the summer months of 2007 and 2008 that have a spatial resolution of 30 m. One Landsat-8 image acquired in summer of 2018 was also used.

The Péiades-1A and -1B are two very high-resolution satellites of the French–Italian Optical and Radar Federated Earth Observation (ORFEO) program. Pléiades-1A was launched in December 2011 and Pléiades-1B was launched in December 2012. They provide Panchromatic, Multispectral, and Bundle products with resolutions of 50 cm, 2 m and 50 cm respectively (Astrium, 2012). This study used multispectral images acquired on 2018-07-26. The images were available for this study because of an affiliation with the Austrian Polar Research Institute (APRI).

Landcover classifications based on Sentinel-1 and Sentinel-2 data were provided by (Bartsch et al., 2019). A combined approach of supervised and unsupervised classification was used to derive the landcover classes from Sentinel-1 VV (IW mode) and Sentinel-2 bands 3 (green, 10 m resolution), 4 (red, 10 m), 8 (near infrared, 10 m), 11 (SWIR, 20 m) and 12 (SWIR, 20 m). Landcover classifications were calculated for nine arctic regions in Russia, Alaska, and Canada . The data set contains landcover results and a signature file for the Maximum Likelihood Classification (Bartsch et al., 2019). The landcover classifications were used to calculate the coastline orientation.

4. Methods

This chapter describes the analysis steps for the study. Section 4.1 explains the preprocessing procedure. The preprocessing was performed twice, once with filtering and once without. Detailed explanations of the threshold classification approach and the erosion rate calculation are given in Sections 4.2 and 4.3.

4.1 Preprocessing

The Sentinel-1, PALSAR-2, and TerraSAR-X data were preprocessed in ESA's SNAP toolbox (ESA, 2019b). The PALSAR data was processed in the ASF MapReady software because of issues with the SNAP tool (ASF, 2019). In general, two different preprocessing approaches were used: one with speckle filtering and one without. The procedure without speckle filtering is described first.

For the procedure without speckle filtering, the first step was radiometrical calibration to convert the intensity values of the image into the backscatter coefficient σ_0.

The second step was multi-looking of the PALSAR-2 and TerraSAR-X images. This step was not necessary for the Sentinel-1 data, because Ground Range Detected (GRD) products were used. GRD products are detected, multi-looked, and projected to ground range using an Earth ellipsoid model (ESA, 2012). Multi-looking was also not performed for the PALSAR images because this capability was not available in the ASF MapReady software.

The third step was ellipsoid correction of the data. For the purposes of this study a terrain correction was not useful, because a precise Digital Elevation Model (DEM) for the constantly changing coastline area was not available. Unfortunately this means that only images with the same orbit constellation are comparable to each other. During the ellipsoid correction, the local incidence angle was extracted.

The final step was converting σ_0 to decibels.

To reduce speckle, a filtering step was added. Again, the first and second steps were radiometrical calibration and multi-looking.

After that, a Lee Sigma filter with the default parameters was applied. (The default parameters are sigma = 0.9, window = 7×7, and target window size = 3×3.) This filter assumes that 95.5% of the pixels are distributed within the two-sigma range from its mean. It replaces the center pixel of a scanning window with the average of those pixels within the two-sigma range of the center pixel. Pixels outside the two-sigma range are not included into the sample mean computing, and a speckle reduction is achieved (Lee et al., 2009).

After that filtering step, the images were ellipsoid corrected and the backscatter coefficient was converted to decibels using the same procedure as the preprocessing without filtering.

The PALSAR data was at first ellipsoid corrected in the ASF MapReady software, and afterwards the Lee Sigma filter was applied in the SNAP toolbox.

4.2 Threshold Classification

For the classification approach, a threshold method with three surface types (water, land and steep cliff) was chosen. The procedure depends on the SAR wavelength. The filtered and unfiltered images were analyzed separately using the same procedure.

4.2.1 Coastline Orientation

As explained in Section 2.2.3, steep coasts that are facing the sensor have a high backscatter coefficient. This is mainly caused by the foreshortening effect and occurs only when the cliff faces the sensor. Therefore it is important for the threshold determination to calculate the angle of the coast relative to the incoming signal.

Calculating the coastline orientation means calculating the intersection angle between the coastline and the line of sight (LOS) of the sensor. The coastline was extracted from a land cover classification provided by Bartsch et al. (2019) and divided into segments with similar orientation. The coordinates of each segment's midpoint and endpoints were calculated.

The midpoints were moved 40 m towards the satellite to test whether the coast was facing toward or away from the satellite. The moved point lies outside the land area if the coastline faces the satellite and inside if it faces away. See Fig. 4.1.

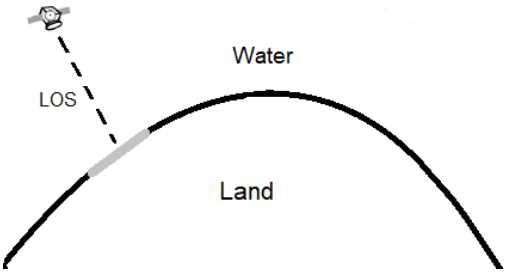

(a) Coastline facing the satellite

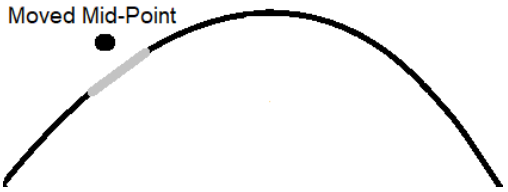

(b) For coastline facing the satellite, moving the midpoint toward the satellite moves it into water

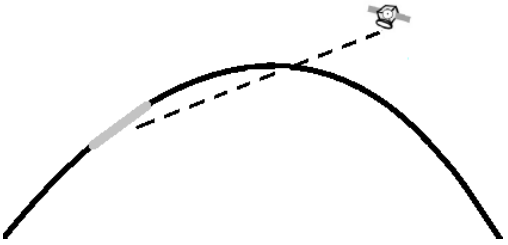

(c) Coastline facing away from the satellite

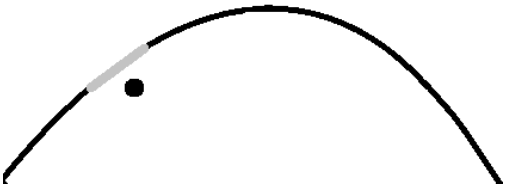

(d) For coastline facing away from the satellite, moving the midpoint toward the satellite moves it into land

FIGURE 4.1: Examples of coastline orientation calculation for coastlines facing the Line of sight (LOS) of a satellite (a and b), and coastlines facing away from the satellite (c and d). The segment is marked in gray.

Finally the incidence angle between the LOS of the sensor and the coast segment was calculated. The gradient of the LOS, m_2, was derived from the inclination of the satellite's orbit. The incidence angle α was calculated

$$\tan \alpha = \frac{m_1 - m_2}{1 + m_1 m_2} \tag{4.1}$$

where m_1 is the gradient of the coast segment. The incidence angles of coast segments facing away from the sensor were increased by 180°.

4.2.2 Determining the Dependence of Backscatter on Incidence Angle

Samples were taken to analyze the dependence of σ_0 on incidence angle for each of the three surface classes (land, water, coast).

The incidence angle range was different for each satellite. The PALSAR/PALSAR-2 range varied from 30° to 42°, Sentinel-1 from 34° to 42.5°, and TerraSAR-X from 19° to 51°.

The samples were visually selected and manually recorded as described in Bartsch et al. (2017). Nearly all images were used, and samples that cover the whole incidence angle range were selected. Images with sea-ice were not used for the water class samples. For the steep coast class, only coasts facing the sensor were sampled. Therefore the coastal sample size was smaller than the land or water sample sizes.

The Sentinel-1 images with an ascending and descending flight direction were separately sampled because of the different sensing times (descending in the morning, ascending in the evening). This may be important, since the wind conditions could differ significantly, which would affect the water conditions and cause different backscatter behaviours. Due to sensor differences, PALSAR and PALSAR-2 images were also sampled separately.

The sample sets were grouped by satellite, surface class, and polarization. Each group was divided into a training set (to calculate the threshold function) and a testing set (to test the quality of the classification results).

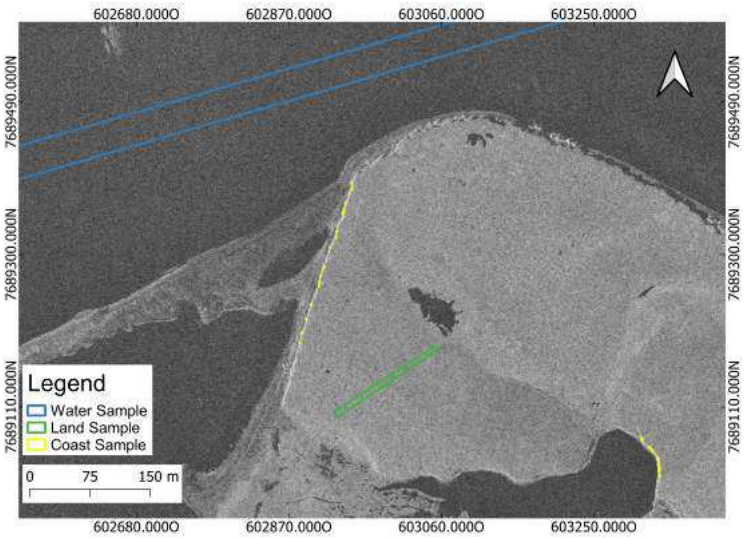

FIGURE 4.2: Example of sampling to determine the dependence of σ_0 on incidence angle. This is a TerraSAR-X image showing the Yukon coast 2018-07-13. The pre-processed TerraSAR-X image lies in the background. Coast samples are displayed in yellow, water samples in blue and land samples in green.

4.2.3 Threshold Calculation and Classification

In order to classify the images, a functional relationship between σ_0 and the incidence angle was calculated. Depending on the surface conditions, different functional relationships can be found in the literature. The incidence angle dependence is often modeled by a linear function (Schlaffer et al., 2016):

$$\sigma_0 = a\theta + b \tag{4.2}$$

However, other models have been used. For example, for the classification of ground-fast and floating ice a third degree polynomial function was found to be the most effective (Bartsch et al., 2017):

$$\sigma_0 = a\theta^3 + b\theta^2 + c\theta + d \tag{4.3}$$

The sample distribution in this study was modeled well with the linear function. The water samples show the lowest backscatter values, and the coast samples the highest. For this reason threshold functions had to be calculated to differentiate the water from land and land from coast (but not water from coast). To derive more precise threshold functions, the standard deviation of the absolute residuals were included. The threshold between water and land was calculated as:

$$\sigma^0_{w/l}(\theta) = \frac{(\sigma^0_{water} + std_{water}) + (\sigma^0_{land} - std_{land})}{2} \tag{4.4}$$

where σ^0_{water} and σ^0_{land} are the function fitted to the water and land samples and their standard deviations are std_{water} and std_{land}. Similarly, the threshold function between the land and coast classes was calculated as:

$$\sigma^0_{l/c}(\theta) = \frac{(\sigma^0_{land} + std_{land}) + (\sigma^0_{coast} - std_{coast})}{2} \tag{4.5}$$

where σ^0_{coast} is the function fitted to the coast samples and its standard deviation is std_{coast}.

These threshold functions were used to classify the image pixels. During the classification process it was calculated whether the σ_0 pixel values lie below or above the threshold functions. If the σ_0 pixel value was below the σ_w/l threshold it was classified as water. Otherwise it was tested whether the σ_0 values lie below or above the σ_l/c threshold. Every pixel above the threshold was classified as steep coast, every value below as land.

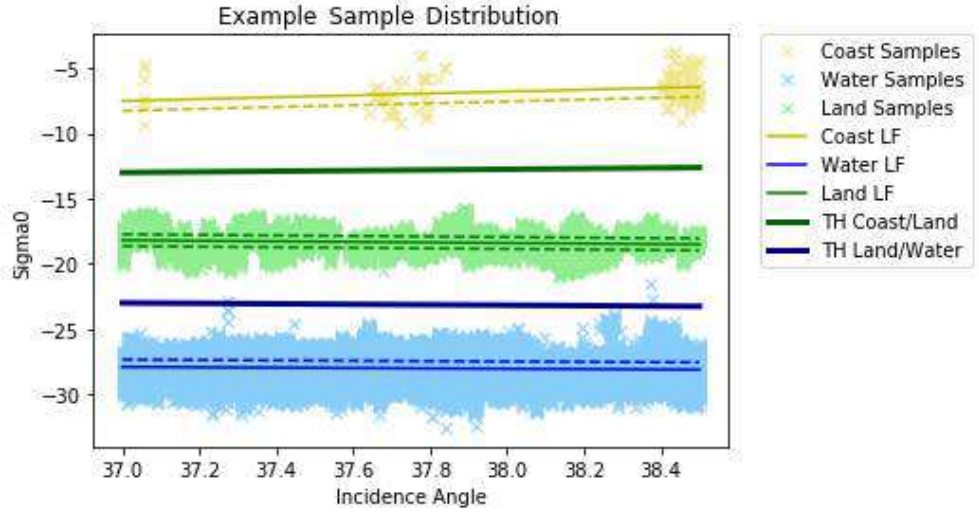

FIGURE 4.3: Threshold calculation example. The fitted linear functions (legend LF) are thin lines and the standard deviations are thin dashed lines. The calculated threshold functions (legend TH) are thick lines.

4.2.4 Error Assessment

The error evaluation was done separately for the different polarizations and for filtered and unfiltered images. The testing set data were classified with the model, and the resulting classes were compared with the land cover from which the data were sampled. At first an error matrix as in 4.1 was produced. Then three error statistics were calculated: the Kappa Coefficient, the "producer's accuracy," and the "user's accuracy."

Error Matrix		Reference Data			
		Coast	**Land**	**Water**	**Total (m)**
Classified Data	**Coast**	a	b	c	a+b+c
	Land	d	e	f	d+e+f
	Water	g	h	j	g+h+j
	Total (n)	a+d+g	b+e+h	c+g+j	

Quality Matrix		Reference Data			
		Coast	**Land**	**Water**	**Users A. (%)**
Classified Data	**Coast**	100	0	0	100
	Land	0	100	0	100
	Water	0	0	100	100
	Total (%)	100	100	100	

TABLE 4.1: Error and quality matrix examples. The error matrix shows the absolute values. In the quality matrix, all values are calculated % and the producer's accuracy is marked in grey.

The Kappa Coefficient evaluates the classification accuracy. It compares how often the results of the classification approach are correct in comparison to an approach that randomly assigns values. It ranges from -1 to 1. -1 means that the classification approach is

significantly worse than the random classification, and 0 indicates that the classification is not significantly better. The Kappa Coefficient is calculated as (Jensen, 2005):

$$\kappa = \frac{n * n_{correct} - n_{incorrect}}{n^2 - n_{incorrect}} \tag{4.6}$$

where n is the total amount of reference data and $n_{correct}$ and $n_{incorrect}$ are the number of samples that are classified correctly and incorrectly.

The producer's accuracy gives the probability that the real surface types are correctly classified in the map. It assesses the fraction of reference data that are classified correctly. Using water as an example, if $n_{correct}$ pixels are correctly classified as water out of n reference water pixels then the producer's accuracy is (Jensen, 2005):

$$ac_{producer} = \frac{n_{correct}}{n}. \tag{4.7}$$

In comparison to the producer's accuracy, the user's accuracy assesses how reliable the classification result is. Again using water as an example, if $n_{correct}$ pixels are correctly classified as water out of m pixels *that the threshold classified* as water then the user's accuracy is (Jensen, 2005):

$$ac_{user} = \frac{n_{correct}}{m}. \tag{4.8}$$

4.3 Coastline Erosion Rates Calculation

Only co-polarized, filtered images were used to calculate the coastal change rates. The rates were calculated for every satellite separately. Table 4.2 gives a summary of the used images and approaches.

PALSAR/PALSAR-2 images between 2007 and 2018 were used to calculate ten-year cliff-top change rates for the west coast of Herschel Island, an area around Kay Point and Bykovsky Peninsula. All images had an ascending pass designation.

PALSAR-2 and Sentinel-1 images between 2017 and 2018 were used to calculated cliff-top change rates at the west coast of Herschel Island and a region around Kay Point. These calculations were done to facilitate comparisons between the sensors.

Sentinel-1 images with descending flight direction were used to calculate coastal changes between 2017 and 2018 based on the boundary between the land and water classification (land–water) at the west coast of Herschel Island. The coastline was not facing the sensor, because of the descending flight direction of the satellite. The results were compared with the calculated cliff-top changes.

For the calculation of the shoreline change rates at the Barents Sea Coast the land–water border was used as coastline. This was done, because there are no steep coasts in the monitored area around Varandey. PALSAR and PALSAR-2 images of 2007 and 2018, and Sentinel-1 and PALSAR-2 images of 2017 and 2018 were used. The Sentinel-1 images had a descending and the PALSAR/PALSAR-2 images an ascending pass designation.

The TerraSAR-X images were used to analyze the seasonal cliff-top changes of an area around the Kay Port between July 2018 and January 2019.

Sensor	Coast	Coastline Type	Time Span
PALSAR/ PALSAR-2	Herschel Island	Cliff-Top	2 & 10 yrs
	Kay Point 1	Cliff-Top	10 yrs
	Bykovsky P.	Cliff-Top	10 yrs
	Barents Sea	Land–Water	2 & 10 yrs
Sentinel-1	Herschel Island	Cliff-Top	2 yrs
		Land–Water	2 yrs
	Barents Sea	Land–Water	2 & 10 yrs
TerraSAR-X	Kay Point 2	Cliff-Top	July–Jan

TABLE 4.2: Summary of the images used for the coastline extraction.

4.3.1 Coastline Extraction

To calculate the exact coastline location, the raster classification results were converted to vector polygons with a script provided by Pointner (2019). Then all polygons were converted to line segments, and the shorelines were manually selected and extracted. For the cliff-top line extraction, only polygons classified as steep coast were analyzed. All landward-lying lines were considered cliff-top lines. For the land–water coastline, the boundary between areas that were classified as land and water was extracted as coastline. A visual comparison with Sentinel-2 and Google Earth optical images was used to orient the terrain and exclude false classification results. Figure 4.4 shows an example of this procedure.

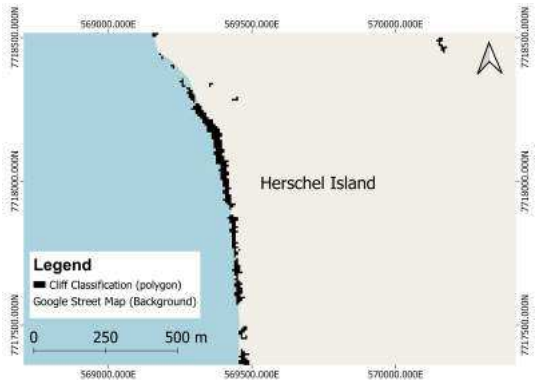

(a) Step 1: Convert raster file to vector polygon.

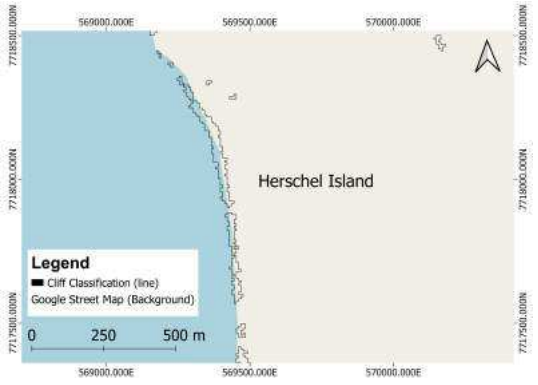

(b) Step 2: Transform polygon to line segments

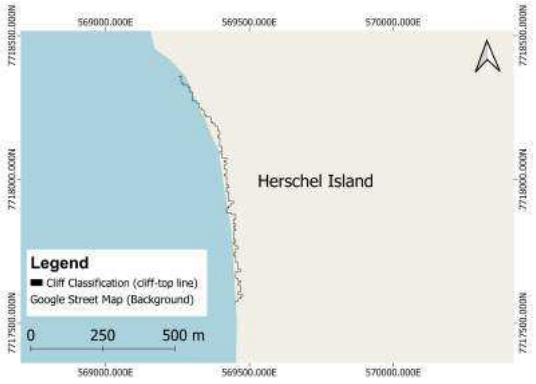

(c) Step 3: Extract cliff-top line.

FIGURE 4.4: Coastline line extraction example. This example is for a cliff-top line, so the landward-lying edges of steep coast polygons are considered the cliff top.

4.3.2 Erosion Rate Calculation

The Digital Shoreline Analysis System (DSAS), an ArcGIS extension provided by the United States Geological Survey (Himmelstoss et al., 2018), was used to derive the coastline erosion rates. DSAS calculates rate-of-change statistics for a chronological series of shoreline vectors. For the erosion rate calculation, baselines and transects were defined as depicted in Fig. 4.5. Based on the spatial resolution, a transect distance of 10 m was used for the PALSAR/PALSAR-2 and Sentinel-1 shorelines, and a distance of 1 m was used for the TerraSAR-X shorelines. The shoreline uncertainty values (*unc*) were chosen to be equal to the spatial resolution of the image (PALSAR and Sentinel-1 20 m, PALSAR-2 10 m, and TerraSAR-X 0.69 m).

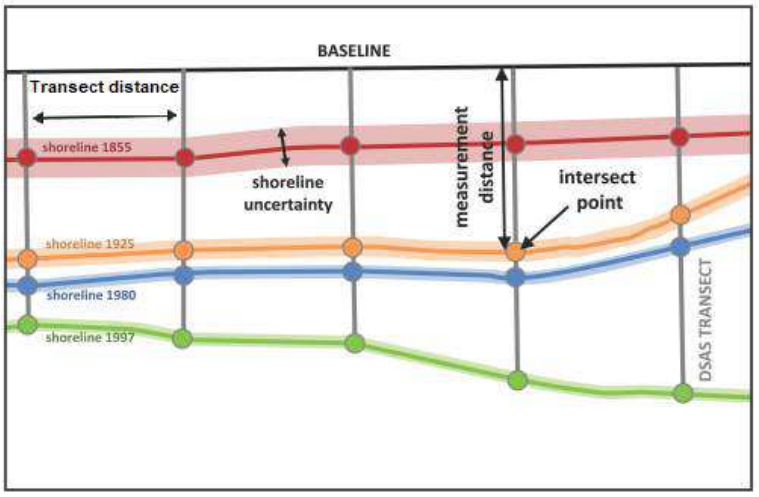

FIGURE 4.5: DSAS example, adapted from source: Himmelstoss et al. (2018)

Three statistics and their uncertainty were calculated: the net shoreline movement (NSM), the end point rate (EPR), and the weighted linear regression (WLR). For the WLR calculation, shorelines from three or more dates are necessary.

The NSM is the distance in meters between the oldest and the most recent shoreline positions for each transect. This NSM value was used to determine the EPR using the calculation (Himmelstoss et al., 2018):

$$EPR = \frac{\text{NSM}}{t_A - t_B} \quad [m/y], \tag{4.9}$$

where $t_A - t_B$ describes the time between the oldest and the most recent shoreline measurements. The uncertainty of the EPR was calculated as:

$$EPR_{unc} = \frac{\sqrt{(unc_A)^2 + (unc_B)^2}}{t_A - t_B} \tag{4.10}$$

where unc_A and unc_B are the uncertainty attribute filed of shoreline A and B.

The WLR was calculated by using least-squares regression to fit a line through the transect points. Data points with a small spatial uncertainty, were given more weight according to the formula (Himmelstoss et al., 2018)

$$w = \frac{1}{unc^2}. \tag{4.11}$$

Like the EPR, the WLR expresses a shoreline change rate for each transect. The EPR is the change between pairs of sequential observations, and the WLR is the overall trend.

The standard deviation for the WLR was calculated as (Himmelstoss et al., 2018):

$$WSE = \sqrt{\frac{\sum (y - y')^2}{n - 2}} \tag{4.12}$$

where y is the observed distance from the baseline for a shoreline data point, y' is predicted value based on the equation of the weighted linear regression and n is the number of dates used. Note that if $n = 2$ the WLR is equivalent to the EPR.

The WLR could only be calculated for the PALSAR/PALSAR-2 shoreline time series because the other datasets only have two timepoints. The NSM and EPR were calculated for the Sentinel-1 and TerraSAR-X data sets. The 2017–2018 EPR for the PALSAR/PALSAR-2 coastlines that overlap with the Sentinel-1 data set were calculated for comparison.

5. Results and Discussion

In Section 5.1 the classification process and its outcomes are reviewed for each satellite and polarization. The coastline erosion rates for the three areas of interest and various satellites are evaluated in Section 5.2. These rates are compared across various satellites and areas of interest in Section 5.3.

5.1 Classification

5.1.1 Coastline Orientation

The steep-coast classification was only performed with images with an ascending flight designation. Therefore, only steep coasts in the areas shown in Fig. 5.1 could be detected with the threshold classification approach. During the steep coast classification three main areas were were identified as steep coasts: the west coast of Herschel Island, an area near Kay Point, and the west coast of Bykovsky Peninsula. In total, 9.6% of Herschel Island's sensor oriented coastline and 40% of the sensor oriented Bykovsky Peninsula coast were classified as steep coast among all of the PALSAR/PALSAR-2 and Sentinel-1 images with an ascending flight designation.

(a) Yukon Coast

(b) Bykovsky Peninsula

FIGURE 5.1: Coastline segments facing the satellites with an ascending flight direction. Only steep coasts in these sensor facing areas can be detected with the threshold classification approach. (The orientations of the images are different.)

5.1.2 Normalized Backscatter Dependence on Incidence Angle

The biggest sample sizes were taken for the water class, the smallest for the steep coast classes. A visual inspection of the sample distribution showed that a linear function was

sufficient to model the relationship between σ_0 and the incidence angle. In the following subsections, the sample distributions for each satellite are analyzed in detail. The term "coast" refers to the steep coast class. Table 5.1 summarizes the parameters of the threshold functions grouped by satellite and polarization.

	Sensor	**Polarization**	**Threshold**	***a***	***b***
Unfiltered	PALSAR-2	HH	Coast–Land	-0.221	4.923
			Land–Water	-0.446	2.062
		HV	Coast–Land	-0.171	-8.181
			Land–Water	-0.263	-16.404
	Sentinel-1	VH	Coast–Land	-0.056	-9.759
			Land–Water	-0.217	-13.819
		VV	Coast–Land	0.059	-7.161
			Land–Water	-0.309	-3.451
	TerraSAR-X	HH	Coast–Land	-0.063	-0.780
			Land–Water	-5.768	-1.660
Filtered	PALSAR-2	HH	Coast–Land	-0.203	4.353
			Land–Water	-0.382	-0.620
		HV	Coast–Land	-0.245	-4.467
			Land–Water	-0.203	-18.753
	Sentinel-1	VH	Coast–Land	-0.055	-9.898
			Land–Water	-0.220	-13.224
		VV	Coast–Land	0.059	-7.266
			Land–Water	-0.303	-3.070
	TerraSAR-X	HH	Coast–Land	-0.023	-2.029
			Land–Water	-1.041	-1.573

TABLE 5.1: Threshold parameters for each satellite and polarization. The parameters a and b refer to Eq. 4.2. PALSAR is omitted because its images were classified based in the PALSAR-2 threshold.

PALSAR/PALSAR-2

The PALSAR and PALSAR-2 samples and linear functions are plotted in Figs. 5.2–5.5. It is important to note that the PALSAR samples cover a smaller range of incidence angles (36° to 40°) than the PALSAR-2 (33° to 42°) samples. The PALSAR threshold function may be inaccurate outside of this range.

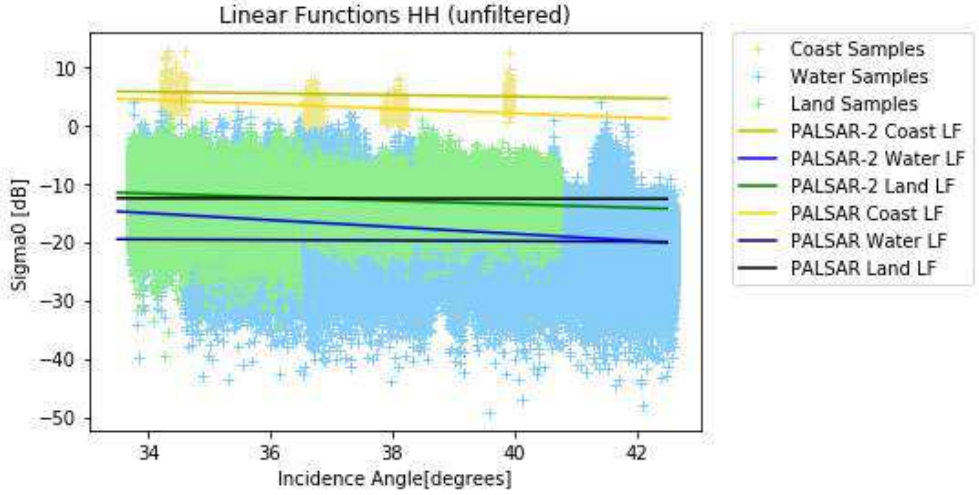

FIGURE 5.2: Unfiltered PALSAR/PALSAR-2 HH-polarization samples and linear fit (LF).

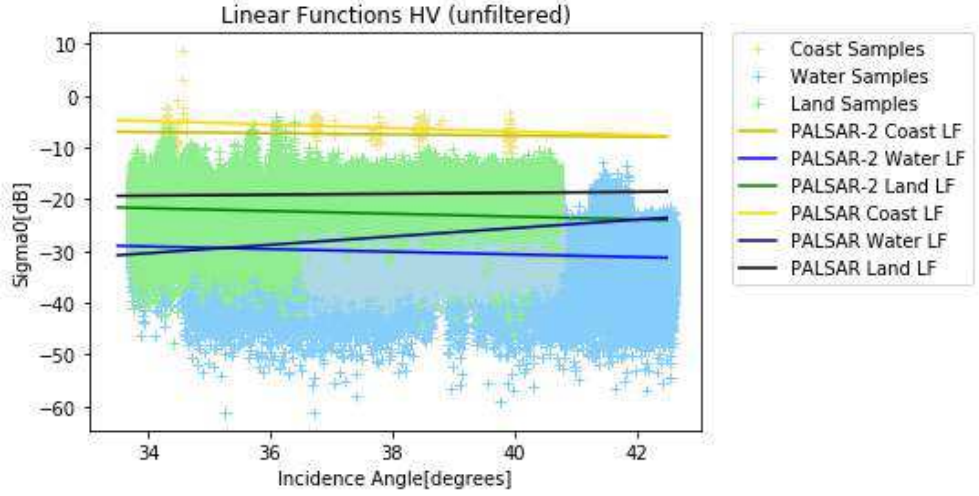

FIGURE 5.3: Unfiltered HV-polarization PALSAR/PALSAR-2 samples and linear fit (LF). PALSAR water samples are highlighted in light blue.

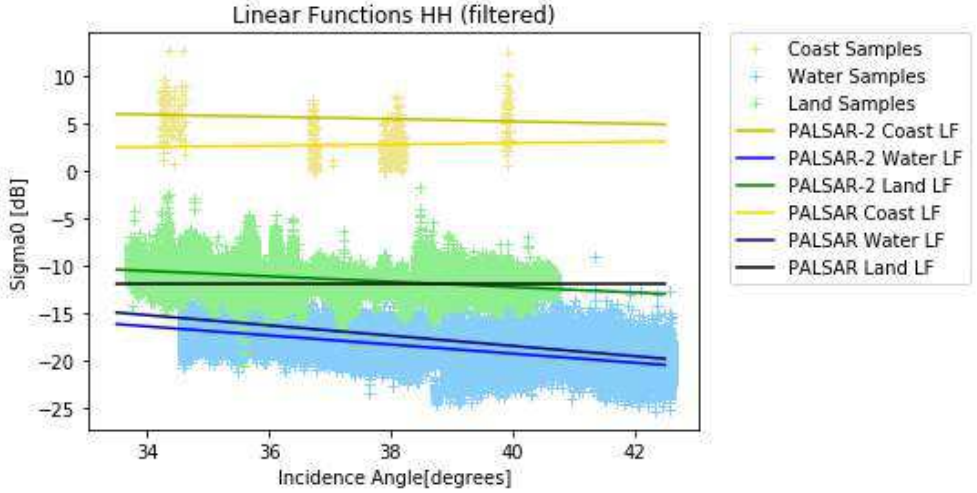

FIGURE 5.4: Filtered HH-polarization PALSAR/PALSAR-2 samples and linear fit (LF).

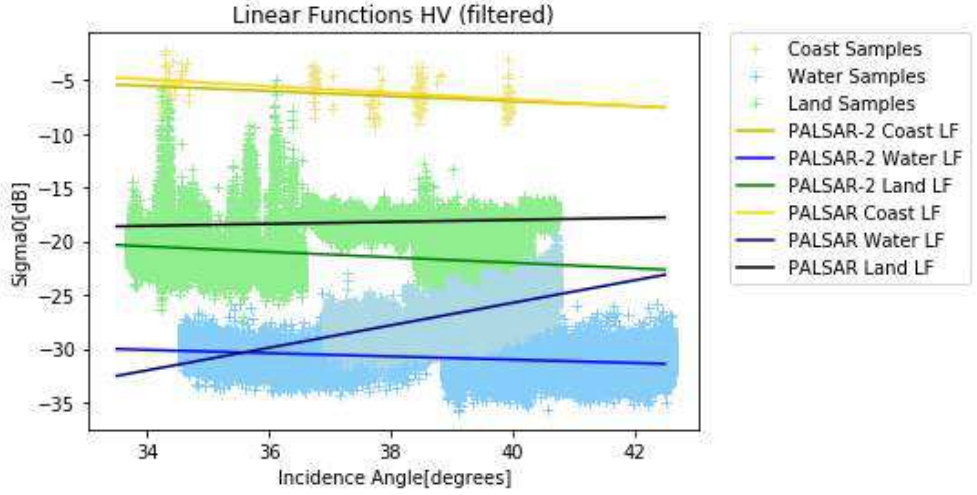

FIGURE 5.5: Filtered HV-polarization PALSAR/PALSAR-2 samples and linear fit (LF). PALSAR water samples are highlighted in light blue.

In general, the PALSAR and PALSAR-2 samples are distributed very similarly. Consistent with preliminary analysis in Section 2.2.3, the coast samples have the highest backscatter values and the water samples have the lowest. The backscatter values of the inland samples lie in between those two. Due to speckle the unfiltered water and land samples are highly variable and the distributions substantially overlap. The filtered samples have a much smaller variance for all classes.

The coast and surface functions for the PALSAR and PALSAR-2 data for both polarizations are very similar. However, the distributions of the water samples in HV

polarization are different between PALSAR and PALSAR-2. See Figs. 5.3 and especially 5.5. One explanation for this is varying water conditions between the sensing times. All PALSAR images were recorded in late August or early September, but the PALSAR-2 images were recorded between the end of June and July. This only affects the HV polarized samples and is not removed by the filtering.

The PALSAR-2 samples were used to calculate the threshold functions for PALSAR and PALSAR-2, because of the higher spatial resolution and wider incidence angle range in the PALSAR-2 data. The threshold functions are plotted in Figs. 5.6–5.7. Although the PALSAR-2 thresholds were used, the PALSAR thresholds are also shown for comparison. Table 5.1 lists the calculated threshold parameters for PALSAR-2.

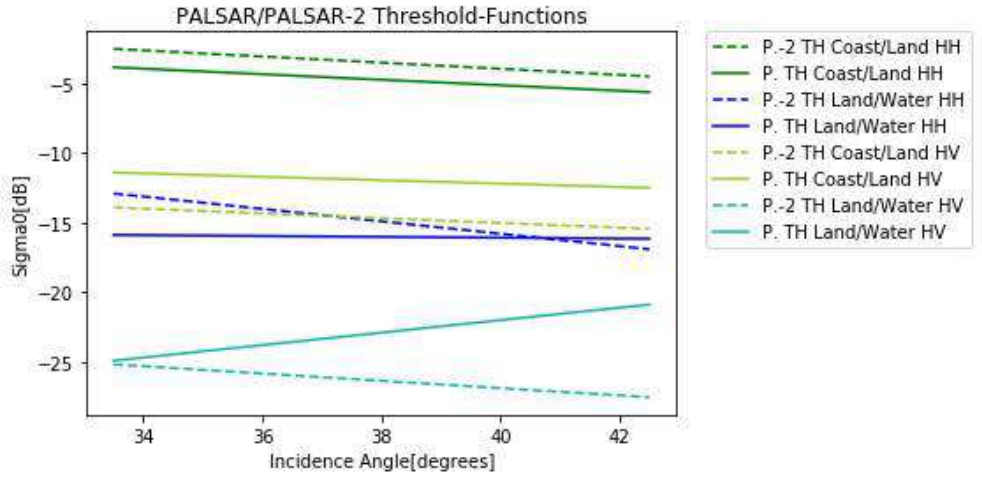

FIGURE 5.6: Unfiltered PALSAR (P) and PALSAR-2 (P2) threshold functions (TH) in HH and HV polarizations. PALSAR thresholds are shown for comparison, but were not used for the classification.

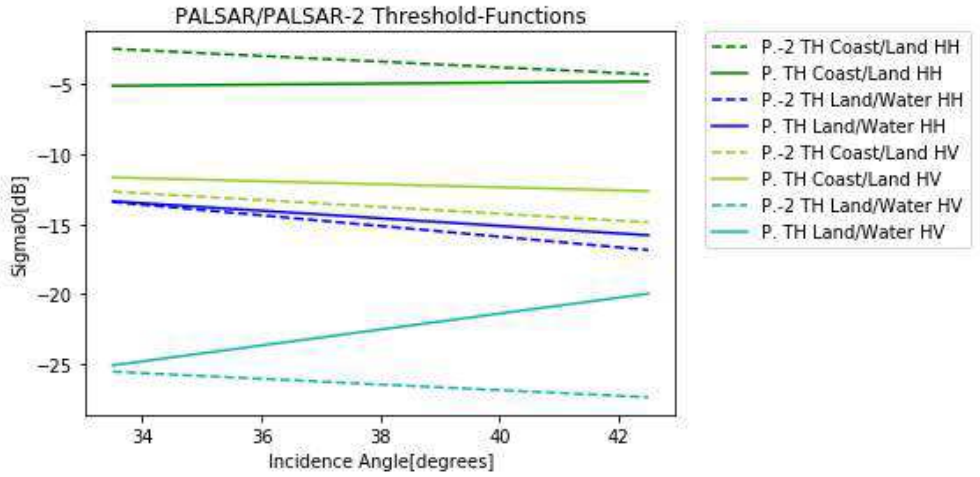

FIGURE 5.7: Filtered PALSAR (P) and PALSAR-2 (P2) threshold functions (TH) in HH and HV polarizations. PALSAR thresholds are shown for comparison, but were not used for the classification.

The influence of the incidence angle on the backscatter values is weak, so a is relatively small. The resulting PALSAR land–water threshold functions are affected by the insufficient number of water samples. Otherwise the PALSAR and PALSAR-2 thresholds are apparently similar. The filtered PALSAR and PALSAR-2 land–water functions in HH polarization (dark blue lines) happen to be closer to each other. The same is also true for the coast–land thresholds in HV polarization (light green lines).

The coast–land threshold function of the unfiltered PALSAR samples in HH polarization (green line in Fig. 5.6) is steeper than the filtered threshold. The PALSAR land–water threshold of the filtered samples in HH polarization (solid blue line in Fig. 5.7) is steeper than the unfiltered threshold (same line in Fig. 5.6). This is probably caused by insufficient samples and not by the incidence angle.

Sentinel-1

The Sentinel-1 images recorded during ascending and descending flight directions were analyzed separately. The steep coast thresholds could only be derived from a small incidence angle range, which may affect the gradient of the linear function outside the sampled range. The samples and linear functions are plotted in Figs. 5.8–5.11.

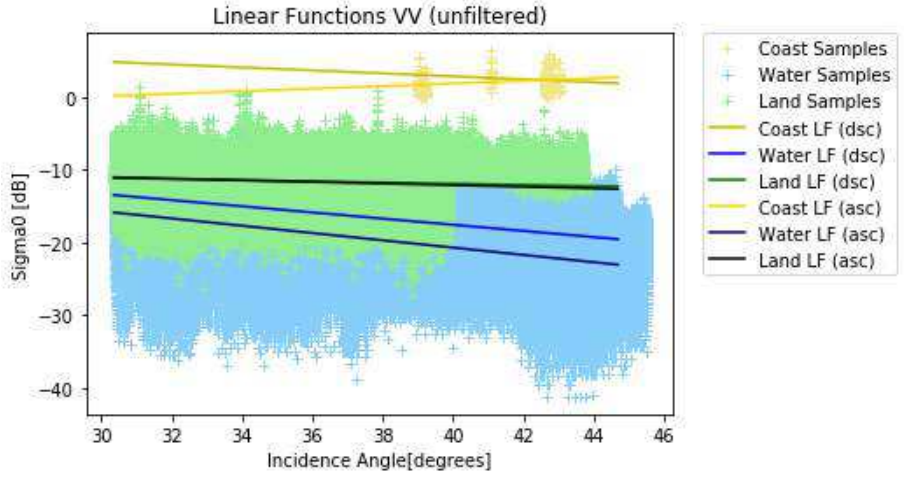

FIGURE 5.8: Distribution of VV-polarization unfiltered ascending (asc) and descending (dsc) Sentinel-1 samples and linear functions (LF).

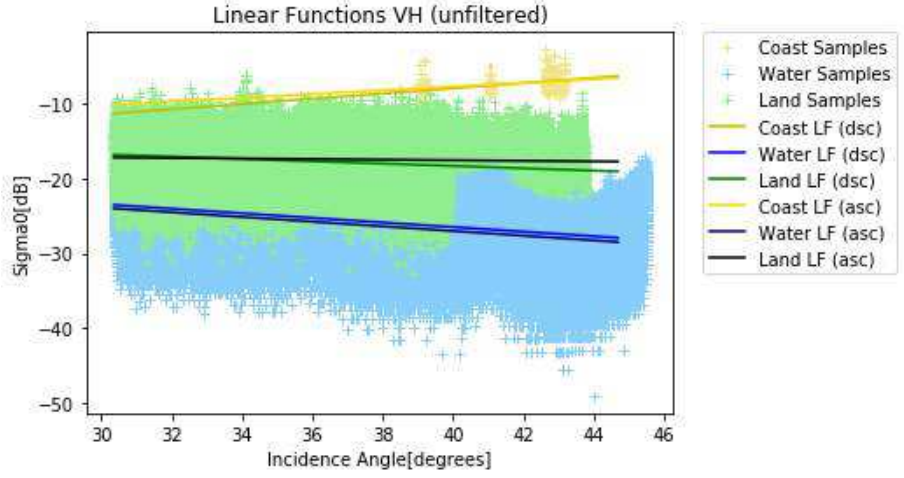

FIGURE 5.9: Distribution of VH-polarization unfiltered ascending (asc) and descending (dsc) Sentinel-1 samples and linear functions (LF).

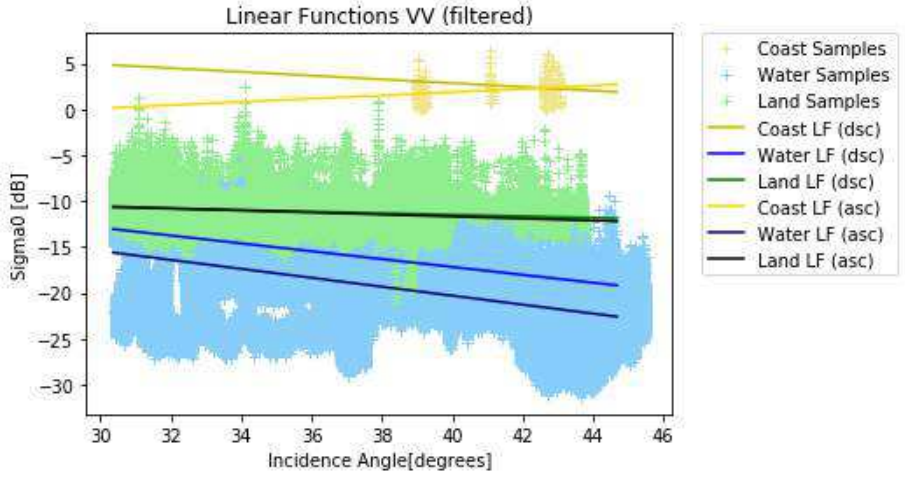

FIGURE 5.10: Distribution of VV-polarization filtered ascending (asc) and descending (dsc) Sentinel-1 samples and linear functions (LF).

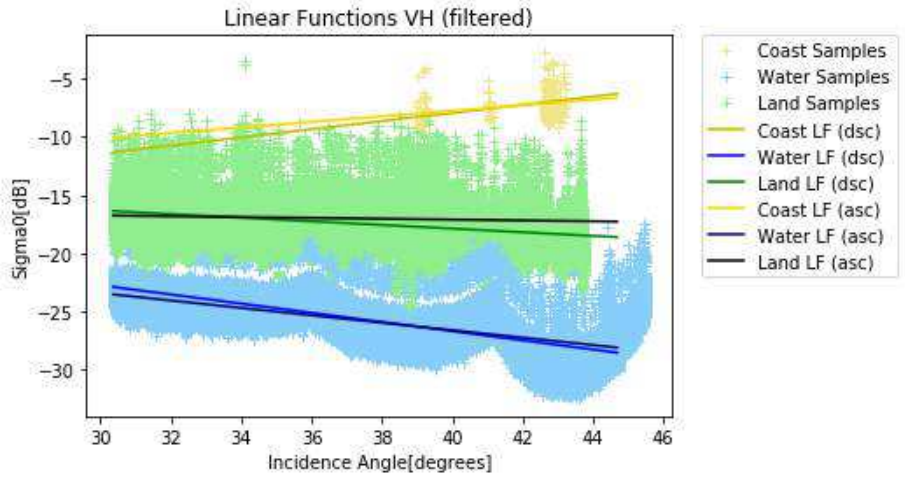

FIGURE 5.11: Distribution of VH-polarization filtered ascending (asc) and descending (dsc) Sentinel-1 samples and linear function (LF).

In general, the HH polarized samples show higher backscatter values than the HV polarized samples, as can be seen in Figs. 5.8–5.11. As with the PALSAR/PALSAR-2 samples, the land and water samples have a high variance, and the classes overlap. After filtering, the variance and overlap are reduced but still present. The incidence angle has a much weaker effect on the backscatter (a is small) for the land and coast classes than the water class. The surprisingly large slope of the coast function in VH polarization (yellow line on Figs. 5.9 and 5.11) is likely caused by an insufficient number of samples or insufficient variety of incidence angles.

The unfiltered and filtered water samples in VH polarization (Figs.5.9 and 5.11) are affected by an intrinsic processing artefact called scalloping effect. This effect causes

wavelike modulation of the image intensity in near-azimuth direction, and could have been reduced with another filtering routine (Romeiser et al., 2013).

A comparison between the ascending and descending linear fit functions shows no significant differences. Therefore, the two data sets were combined for the threshold calculation. The threshold functions are plotted in Figs. 5.12 and 5.13 and the parameters are listed in Table 5.1. The ascending and descending thresholds are plotted separately to show their similarity, but the combined threshold function is listed in Table 5.1 and used in later analysis.

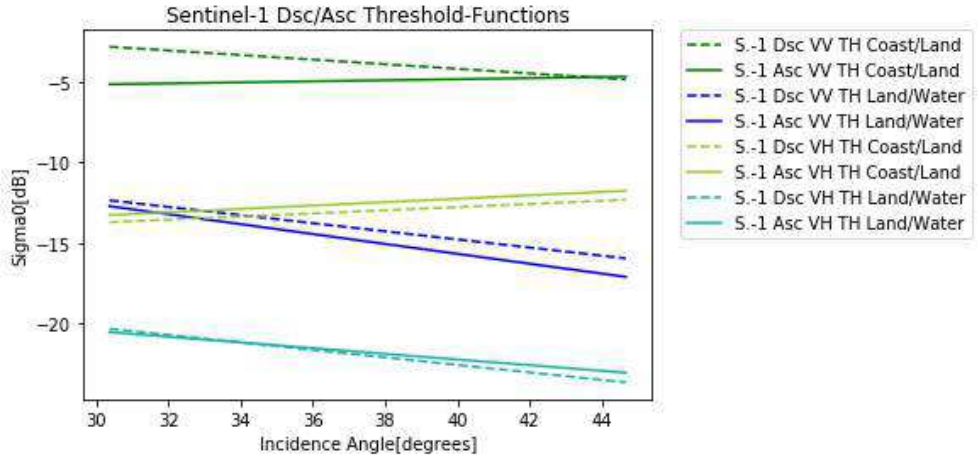

FIGURE 5.12: Unfiltered Sentinel-1 (S.-1) ascending (asc) and descending (dsc) threshold functions (TH) in VV and VH polarizations.

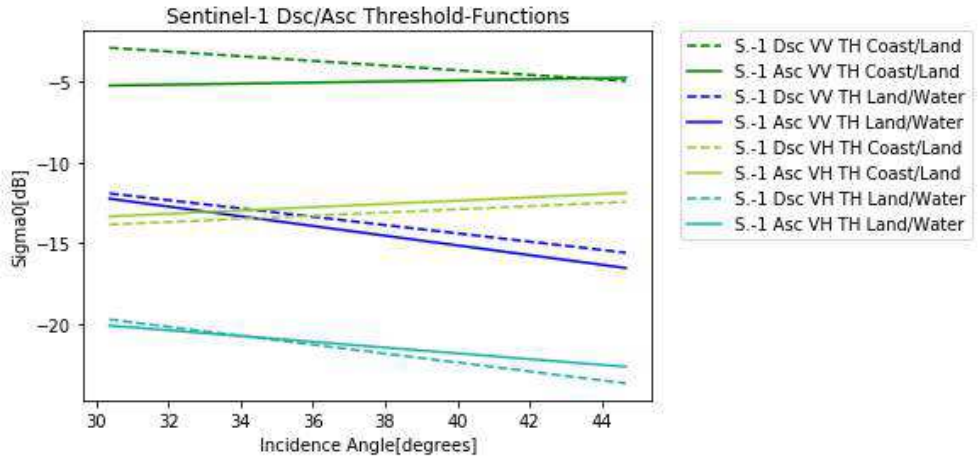

FIGURE 5.13: Filtered Sentinel-1 (S.-1) ascending (asc) and descending (dsc) threshold functions (TH) in VV and VH polarizations.

The resulting threshold functions of filtered and unfiltered samples are very similar. However, the filtered water samples are affected more by the scalloping effect, so the

ascending and descending threshold functions from unfiltered samples are slightly closer together (cyan lines in Figs. 5.12 and 5.13).

TerraSAR-X

The TerraSAR-X samples cover the widest incidence angle range (19° to 51°), but because of a limited number of images, sample gaps exist. The images with an incidence angle around 51° show no steep coasts. For this reason, steep coast samples only exist for incidence angles between 19° and 40°.

Like the other satellites, the unfiltered sample values have high variance, and the water and land samples overlap. Filtering reduces the spread, but the water and land samples still overlap for incidence angles around 50°. The backscatter values are barely affected by the incidence angle (so a is small). The water samples show slightly higher backscatter values for larger incidence angles ($a > 0$), but this is likely caused by sampling from particular areas and not a direct effect of the incidence angle.

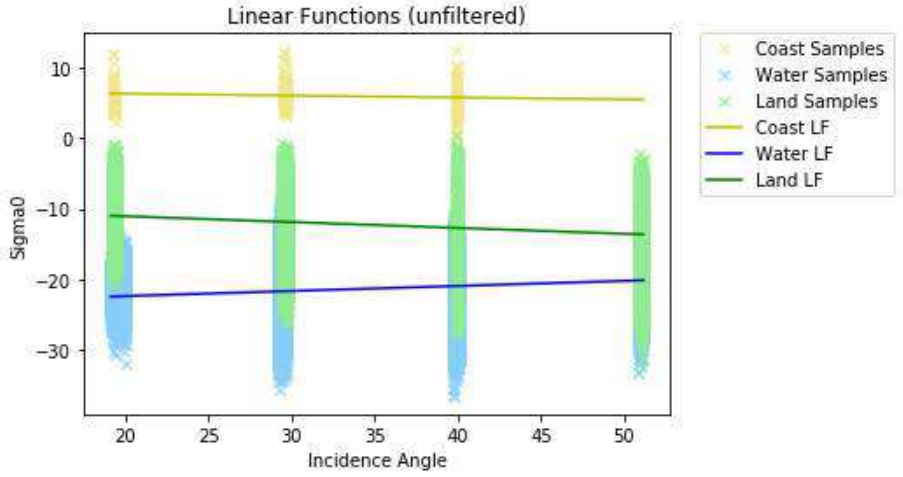

FIGURE 5.14: Sample distribution and linear function (LF) of unfiltered TerraSAR-X samples in HH polarization.

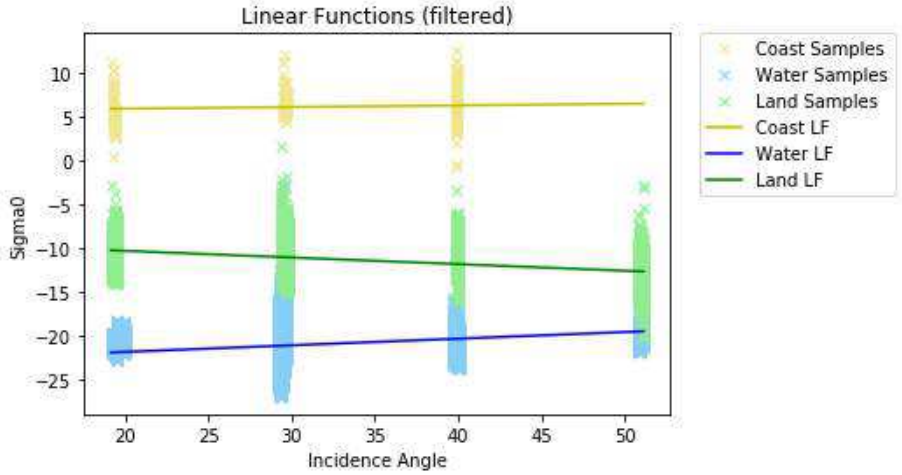

FIGURE 5.15: Sample distribution and linear function (LF) of filtered TerraSAR-X samples in HH polarization.

The threshold functions calculated from the TerraSAR-X data are plotted in Fig. 5.16. A comparison of the threshold functions shows subtle differences. Filtering increases the water–land threshold (blue lines). The filtering step also leveled the coast–land function (green line), which indicates that the slope of the unfiltered threshold functions are more likely statistical noise from speckle than significant effects of the incidence angle.

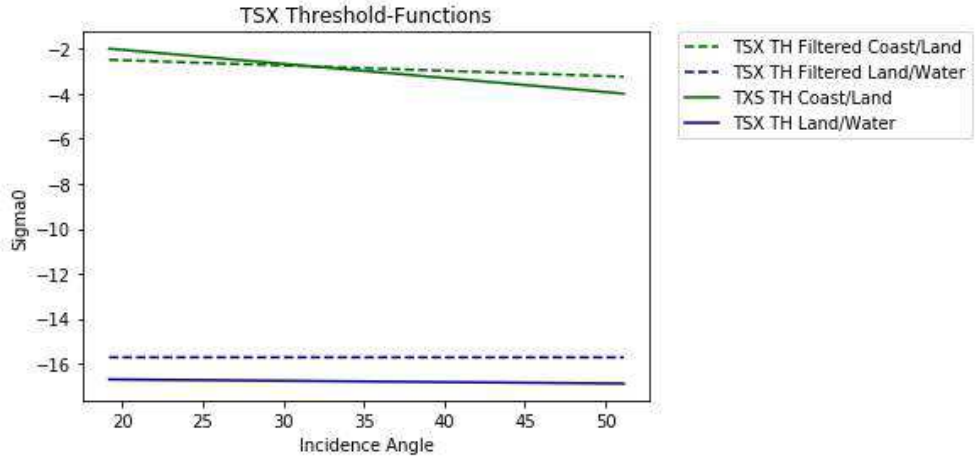

FIGURE 5.16: Filtered and unfiltered TerraSAR-X (TSX) threshold functions (TH) in HH polarization.

5.1.3 Error Assessment

In this section, detailed satellite-by-satellite values of the user's and producer's accuracy are given first. Comparisons of the Kappa Coefficient are listed for a comparison of the senors.

PALSAR and PALSAR-2

The classification errors for PALSAR and PALSAR-2 are listed in Tables 5.2 and 5.3.

PALSAR/PALSAR-2 HH (unfiltered)		Reference Data			
		Coast	**Land**	**Water**	**Users A. (%)**
Classified Data	**Coast**	100	0.23	0	71.39
	Land	0	82.39	17.08	49.93
	Water	0	17.38	82.92	95.85
	Total (%)	100	100	100	

PALSAR/PALSAR-2 HV (unfiltered)		Reference Data			
		Coast	**Land**	**Water**	**Users A. (%)**
Classified Data	**Coast**	100	3.20	0	7.68
	Land	0	87.71	28.72	38.7
	Water	0	9.09	71.28	97.43
	Total (%)	100	100	100	

TABLE 5.2: PALSAR and PALSAR-2 quality matrices for unfiltered test-samples grouped by polarization. The producer's accuracy values are highlighted in grey. All values are in %.

PALSAR/PALSAR-2 HH (filtered)		Reference Data			
		Coast	**Land**	**Water**	**Users A. (%)**
Classified Data	**Coast**	100	0	0	100
	Land	0	28.49	0.30	93.70
	Water	0	71.51	99.7	87.18
	Total (%)	100	100	100	

PALSAR/PALSAR-2 HV (filtered)		Reference Data			
		Coast	**Land**	**Water**	**Users A. (%)**
Classified Data	**Coast**	100	0.03	0	88.34
	Land	0	77.14	14.14	52.76
	Water	0	22.83	85.86	94.84
	Total (%)	100	100	100	

TABLE 5.3: PALSAR and PALSAR-2 quality matrices for filtered test-samples grouped by polarization. The producer's accuracy is highlighted in grey. All values are in %.

The producer's accuracy of the steep coast classification is 100% for every polarization, filtered or unfiltered data. In other words, every coast pixel in the testing data was classified correctly. The user's accuracy for identifying coastal pixels is between 71% and 100% because some land pixels were incorrectly classified as coast. The unfiltered HV polarization classifications are unusually poor, with a user's accuracy of only 7.68%. In this case, 3.20% of all land pixels were misclassified as steep coast. The best result for coast classifications was the filtered HH threshold function.

The producer's accuracy for land is between 77% and 88%, except for the filtered HH-polarized data. Here, the producer's accuracy is only 28.49%. In general, filtering decreases the producer's accuracy of the land classifications. The filtering process seems

to reduce the overall backscatter values of the land samples, because the filtered land pixels were mostly misclassified as water. However, filtering improves the user's accuracy.

The results for the water classification show tendencies opposite to the land class. The water producer's accuracy values vary between 71% and 100%, and they improve after filtering. The user's accuracy decreases after filtering process. This is caused by the increased misclassification of land samples as water.

Among all classes, the filtered HH-polarized threshold functions show the most accurate classification results.

Sentinel-1

The classification errors for Sentinel-1 are listed in Tables 5.4 and 5.5.

Sentinel-1 VV (unfiltered)		Reference Data			
		Coast	**Land**	**Water**	**Users A. (%)**
Classified Data	**Coast**	100	0.19	0	12.71
	Land	0	88.73	10.09	57.43
	Water	0	11.08	89.91	98.15
	Total (%)	100	100	100	

Sentinel-1 VH (unfiltered)		Reference Data			
		Coast	**Land**	**Water**	**Users A. (%)**
Classified Data	**Coast**	100	2.21	0	1.5
	Land	0	61.20	0	99.96
	Water	0	36.59	100	96.04
	Total (%)	100	100	100	

TABLE 5.4: Quality matrices for Sentinel-1 test-samples, with VV polarization above and VH below. The producer's accuracy is highlighted in grey. All values are in %.

Sentinel-1 VV (filtered)		Reference Data			
		Coast	**Land**	**Water**	**Users A. (%)**
Classified Data	**Coast**	100	0.13	0	18.39
	Land	0	97.56	4.13	78.47
	Water	0	2.31	95.87	99.63
	Total (m)	100	100	100	

Sentinel-1 VH (filtered)		Reference Data			
		Coast	**Land**	**Water**	**Users A. (%)**
Classified Data	**Coast**	100	0.43	0	7.32
	Land	0	66.34	0	100
	Water	0	33.23	100	95.13
	Total (%)	100	100	100	

TABLE 5.5: Quality matrices for filtered Sentinel-1 test-samples, with VV polarization above and VH below. The producer's accuracy is highlighted in grey. All values are in %.

All Sentinel-1 coast test-samples were classified correctly. However, the user's accuracy values, ranging from 2% to 18%, are relatively low. Filtering improves the user's accuracy somewhat. Independent from the polarization or filtering, only land samples were misclassified as steep coast. This may be caused by inland mountains or hills, which, also effected by the foreshortening effect, have high backscattering values.

The producer's accuracy for unfiltered and filtered land samples in VV polarization is 88.73% and 97.56%, respectively. The producer's accuracy for unfiltered land samples is lower with 61.20% and 66.34%, respectively. The misclassification of land as water occurs more often for VH polarizations and when filtering is not used. Simultaneously, the user's accuracy of the land class is lower for VV polarizations (57.43% and 78.47%) because water is misclassified as land.

Except for this effect, the results for the water classification show no anomalies. The user's accuracy is between 96% and 100%. The producer's accuracy is between 89% and 98% for VV samples and 61% to 62% for VH samples.

The best overall performance, with $\kappa = 96.07\%$, was achieved with the filtered, co-polarized threshold functions. The performance of the unfiltered cross-polarized threshold functions was slightly worse, with $\kappa = 95.94\%$.

TerraSAR-X

The classification errors for TerraSAR-X are listed in Table 5.6.

TerraSAR-X (unfiltered)		Reference Data			
		Coast	**Land**	**Water**	**Users A. (%)**
Classified Data	**Coast**	100	0.07	0	71.20
	Land	0	88.25	10.81	60.70
	Water	0	11.68	89.19	97.58
	Total (%)	100	100	100	

TerraSAR-X (filtered)		Reference Data			
		Coast	**Land**	**Water**	**Users A. (%)**
Classified Data	**Coast**	100	0	0	100
	Land	0	99.87	0.60	97.41
	Water	0	0.13	99.4	99.97
	Total (%)	100	100	100	

TABLE 5.6: TerraSAR-X Quality matrices for filtered and unfiltered test-samples. The producer's accuracy is highlighted in grey, and all values are in %.

The filtered TerraSAR-X threshold functions show the best overall performance. All steep cost samples were classified correctly. The user's accuracy of the threshold functions for coast pixels is 71.20% without filtering and 100% with filtering. Unlike other satellites, no water pixels were misclassified as coast. Without filtering, 12% of the land pixels were misclassified as water, and this improves with filtering to 0.13%. The user's

accuracy is between 61% (unfiltered) to 97%. The producer's and user's accuracy for the water samples were high, between 89% and 100% for all cases.

Sensor Comparison

All steep coast samples were correctly classified as steep coast, regardless of sensor or filtering. This is especially important for assessing coastal erosion, where a systematic estimate of the coastline is needed. Water–land and coast–land misclassification occurs, but this probably will not affect the erosion analyses based on the extraction of steep coasts. However, the approach based on the land–water border could be affected by this.

The Kappa Coefficients for all results are between 73% and 99%. These values indicate that the classification results are relatively accurate. A comparison between the filtered and unfiltered results shows that filtering almost always improved the classification, regardless of satellite and polarization. The exception was the Sentinel-1 VH polarization, for which the classification results with unfiltered test-samples yield slightly higher Kappa Coefficients. This may be caused by the scalloping effect. In general the filtering step reduces speckle, which led to better classification results in this study. However, pixel information (backscatter information) is lost and blur effects can occur because of filtering (Stettner et al., 2017).

The highest Kappa Coefficients were achieved with the filtered classifications of TerraSAR-X data. This result is not surprising because of the high resolution of the TerraSAR-X images. The PALSAR/PALSAR-2 classifications yield the lowest Kappa Coefficients, but the producer's and user's accuracy values are still high. Overall, threshold functions calculated with co-polarized, filtered samples yielded the highest classification accuracy.

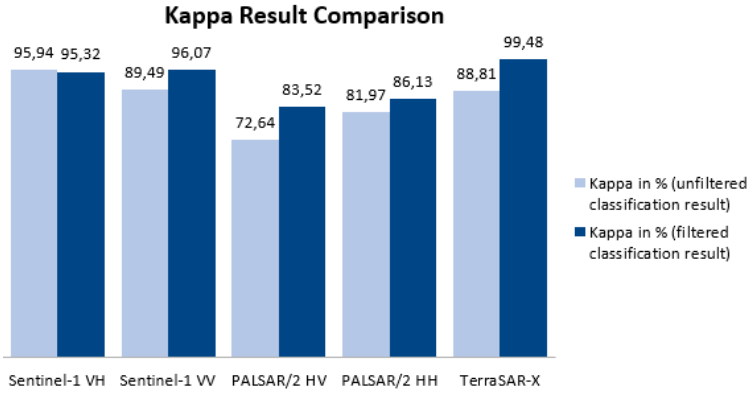

FIGURE 5.17: Kappa Coefficient (%) comparison of the classification results. PALSAR/2 was used as an abbreviation for PALSAR and PALSAR-2.

5.1.4 Classification Issues

In addition to the split-sample error assessment reported in the previous section, the classification results were visually compared to Google Earth, Sentinel-2, and Landsat images to identify possible classification errors and their causes.

The TerraSAR-X classification results show seasonal challenges associated with wet snow. Fig. 5.18 shows TerraSAR-X classification results at the Yukon Coast near King Point one month apart. The red polygons in Figs. 5.18b and 5.18d show an area where some pixels were classified as water based on SAR data from 2018-06-15 but classified as land and steep coast from the 2018-07-29 SAR data. A comparison with the Sentinel-2 optical images reveals that this area is land. On 2018-06-15 snow and ice were still covering the surface, but by 2018-07-29 the snow and ice is mostly thawed. The mean temperature around 2018-06-15 in that area hovered slightly above 0°C (Government Canada, 2019). This indicates, that the snow was melting. Like offshore water, wet snow typically absorbs the microwave signal and reduces the backscatter intensity significantly (Antonova et al., 2016), which caused the false classification result.

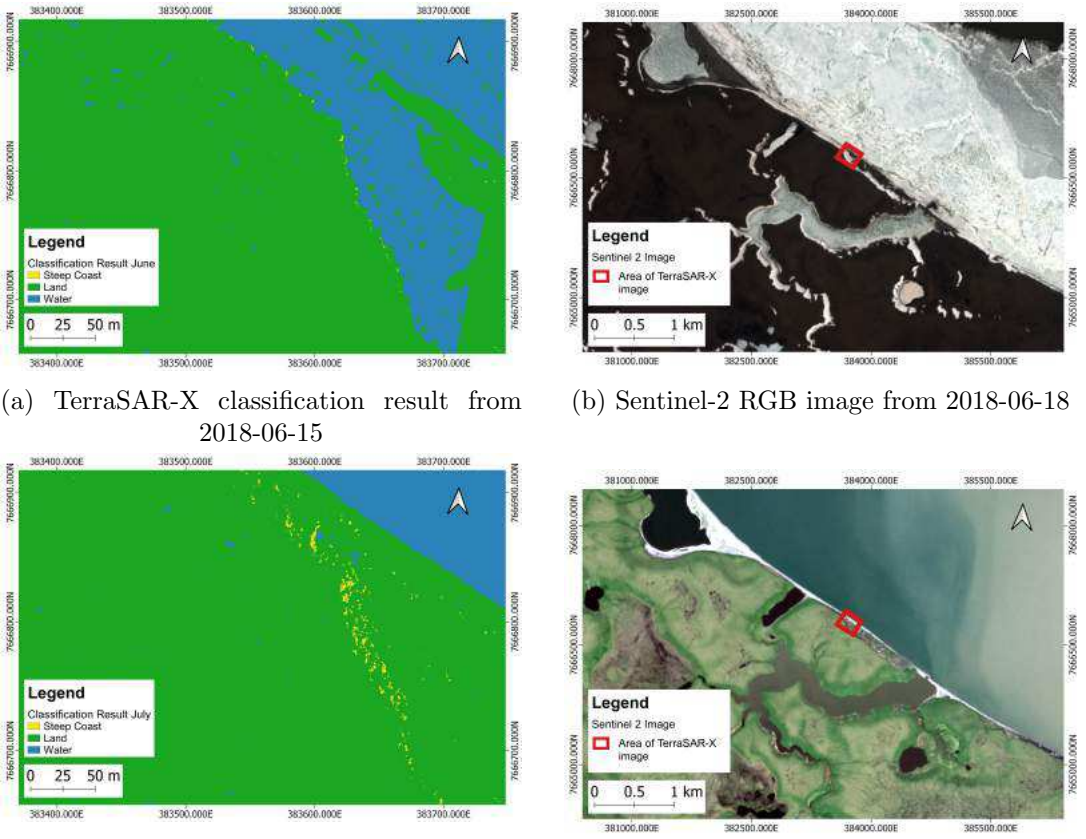

(a) TerraSAR-X classification result from 2018-06-15

(b) Sentinel-2 RGB image from 2018-06-18

(c) TerraSAR-X classification result from 2018-07-29

(d) Sentinel-2 RGB image from 2018-07-24

FIGURE 5.18: The influence of snow and ice on the classification result in TerraSAR-X. The locations of a) and c) are marked as red rectangles in b) and d).

Stettner et al. (2018) analyzed the use of TerraSAR-X images for snowmelt monitoring in the arctic. They determined that snowmelt was best identified using images in VH polarization. A threshold of 1 db was found to give reasonable results to measure the variability of the snow cover extent (Stettner et al., 2018). Future studies about seasonal coastline changes in the arctic could use this threshold in their classification process to detect wet snow that would cause land–coast–water misclassifications.

Wide, smooth sand beaches are also difficult to classify, especially for longer wavelengths. Figure 5.19 shows a smooth sand beach that C- and L-band data indicates is water. The classification result of the shorter C-band wavelength is slightly better. The roughness of the material in comparison of the wavelength is the main factor whether a specular reflection or a scattering of the wave takes place (Jones and Vaughan, 2010). Like calm water, sand is a relatively smooth surface in comparison to the C- and L-band wavelengths, and the microwave signal is reflected in a single beam that is not directed toward the sensor. Furthermore, the radar backscatter depends on the geometric and dielectric properties of the surface. Sand has in general a very low dielectric constant, so the microwaves penetrate deep into the material. This reduces the backscatter signal even more (Stephen and Long, 2005). This makes SAR classification of sandy areas, like parts of the Barents Sea coast, challenging.

Banks et al. (2014) analyzed the backscatter characteristics of Arctic shore and near-shore landcover types for C-band images in various incidence angle ranges and polarizations. They found that the separability between sand and water backscatter in C-band strongly depends on the incidence angle and polarization. The best separability was given with images in HH polarization with shallow (45.3°–49.5°) and medium (39.3°) incidence angles. However, images with steep (20.9°–24.2°) incidence angles tend to bring better separability results in VV and HV polarizations (Banks et al., 2014). Based on these findings, a new polarization and incidence angle dependent threshold function between water and sand could be included into the classification approach. This might improve the classification accuracy in sand areas.

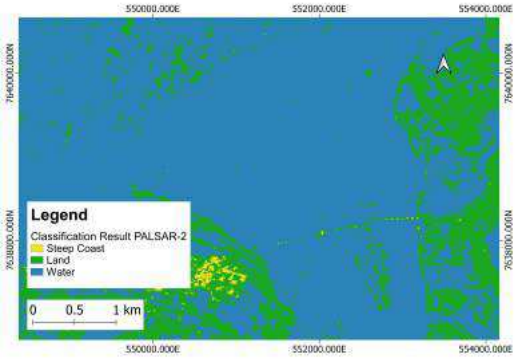

(a) Classification result of PALSAR-2 data recorded 2018-07-14

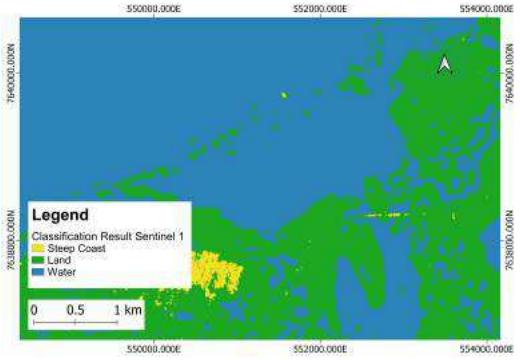

(b) Classification result of Sentinel-1 data recorded 2018-07-23

(c) Google Earth Image captured in 2019, source: Google

FIGURE 5.19: Example of PALSAR/PALSAR-2 and Sentinel-1 misclassification of sandy beach as water. All three images are the same sandy beach location near Varandey. SAR data are classified as land (green), steep coast (yellow), or water (blue).

Misclassifications are also caused by infrastructure. Buildings show high backscatter values due to foreshortening and the double-bounce effect. Smooth streets scatter almost no signal back toward the sensor (Balz and Liao, 2010). This causes misclassifications of buildings and metallic objects as steep coast and misclassifications of streets as water. Two examples from this study are shown in Fig. 5.20. In this study, building misclassifications only affected the erosion analysis at the tip of Bykovsky Peninsula (Fig. 5.20a). In this area the buildings are relatively near at the cliffs, and the low-resolution SAR data cannot distinguish the cliff from the infrastructure. In the Barents Sea area (Fig. 5.20c) the infrastructure misclassifications did not affect the erosion analysis because the coast is not a steep cliff. (The land–water border was used as the coastline for the erosion analysis.)

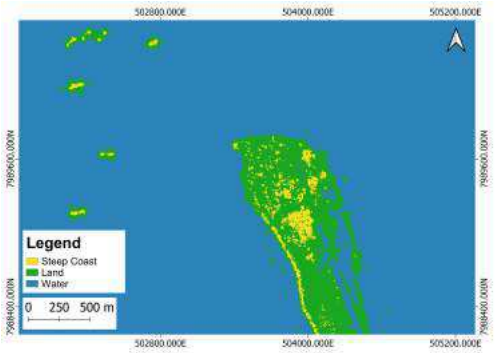

(a) Classification result from PALSAR-2 data captured 2018-08-07

(b) Sentinel-2 RGB image captured 2018-08-28

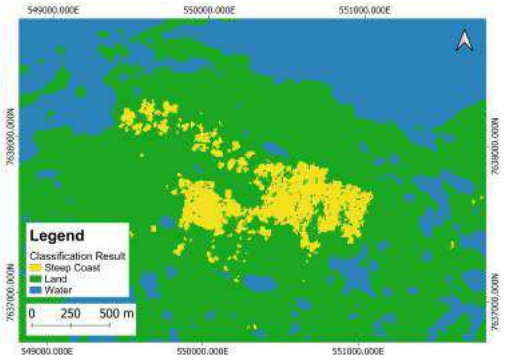

(c) Classification result from Sentinel-1 data captured 2018-07-23

(d) Google Earth image captured in 2019, source: Google

FIGURE 5.20: Results where infrastructure was misclassified as steep coast and water. SAR data are classified as land (green), steep coast (yellow), or water (blue).

5.2 Coastline Erosion Rates

This section reports three different erosion rate estimates. The "mean rate of change" summarizes the change of all segments together, while the "erosion rate" and "accretion rate" are the average change of just the eroding and accreting segments, respectively. Table 5.7 summarizes the calculated erosion rates. Most of the results show negative mean change rates, which indicates that the areas were predominately eroding. The calculated rates for the same regions based on images from different sensors are very similar. However, the uncertainty values of the PALSAR-2 and Sentinel-1 results are high. The spatial resolution also affects which erosion processes can be monitored. Choosing a transect distance much lower than the spatial resolution will not improve the calculation results. Therefore, only erosion features larger or equal to the spatial resolution of the image can be captured.

Region	Sensor	Coastline Type	Years	Mean Change Rate m/year	Mean Erosion Rate m/year	Mean Accretion Rate m/year
Herschel Island	P., P.-2	Cliff-Top	07–18	-0.83 ± 0.87	2.24	1.04
	P.-2	Cliff-Top	17–18	-0.18 ± 8.19	9.9	6.68
	S.-1	Cliff-Top	17–18	0.9 ± 16.02	9.4	9.96
	S.-1	Land–Water	17–18	-9.28 ± 16.56	24.27	17.18
Kay Point	P., P.-2	Cliff-Top	07–18	0.55 ± 1.00	0.62	3.14
	TSX	Cliff-Top	18–19[a]	-0.03 ± 0.90	1.29	2.11
Bykovsky Peninsula	P., P.-2	Cliff-Top	07–18	-0.93 ± 0.29	1.88	0.83
Barents Sea Coast	P., P.-2	Land–Water	07–18	-5.41 ± 3.03	5.41	None
	P.-2	Land–Water	17–18	-2.51 ± 17.55	11.64	7.53
	S.-1	Land–Water	17–18	-3.00 ± 28.68	9.53	12.23

Footnote *a*: Classified data spanned July 2018 to January 2019.

TABLE 5.7: Summary of the shoreline movement results grouped by region. The shoreline movements were calculated based on PALSAR (P.), PALSAR-2 (P.-2), Sentinel-1 (S.-1), and TerraSAR-X (TSX) image classifications. A mean change rate <0 indicates erosion.

The following subsections provide detailed results for each region. For various regions of the Yukon Coast, images from one or more satellites were available. This made it possible to calculate seasonal changes between July 2018 and January 2019 with TerraSAR-X images (Section 5.2.1) and 10-year rates with PALSAR/PALSAR-2 images (Section 5.2.2). For the Herschel Island region of the Yukon Coast, 10-year rates were calculated with PALSAR/PALSAR-2 images and compared to annual changes between 2017 and 2018 calculated with PALSAR-2 and Sentinel-1 images (Section 5.2.3). Along the Yukon Coast, both the cliff-top line and the land–water border were used to calculate the erosion rates.

For the Bykovsky Peninsula (Section 5.2.4) and Barents Sea Coast (Section 5.2.5), less data was available. Only 10-year changes could be calculated for the Bykovsky Peninsula and only 10-year and annual changes for the Barents Seas Coast. Cliff-top lines along the Bykovsky Peninsula and the land–water border along the Barents Sea Coast were used to calculate the respective erosion rates.

5.2.1 Yukon Coast: Kay Point Seasonal Changes

Seasonal net shoreline movements were calculated for the four areas around Kay Point marked in Fig. 5.21. Table 5.8 summarizes the calculated rates for the different areas. The rate of change was calculated on 752 transects. Among these, 258 had a non-zero change. The average change rate of all transects was -0.03 ± 1.30 m/year. Only one area, Area 3, had a positive change rate (1.23 ± 1.80 m/year). All the other areas showed slightly negative rates (between -0.02 and -0.98 ± 1.80 m/year). Only 15.50% of the transects showed statistically significant erosion rates, with a maximum erosion rate of -5.92 m/year in Area 4. The average erosion rate is 1.29 m/year. Slightly more of the transects (18.99%) showed statistically significant accretion, with an average rate of 2.11 m/year.

FIGURE 5.21: Yukon Coast shorelines extracted from 2018–2019 TerraSAR-X data with the four areas marked. The background is a Sentinel-2 RGB image.

Area	Coastline Type	Mean Change Rate m/year	Mean Erosion Rate m/year	Mean Accretion Rate m/year
1	Cliff-Top	-0.02 ± 1.80	1.42	2.32
2		-0.08 ± 1.80	0.88	0.78
3		1.23 ± 1.80	1.01	2.67
4		-0.98 ± 1.80	1.08	0.44

TABLE 5.8: Summary of the Kay Point seasonal shoreline movements calculated with TerraSAR-X image classifications. A mean change rate < 0 indicates erosion.

In general, more steep coast regions could be identified from the summer SAR data. This indicates that the dielectric properties of the surface strongly affect the backscatter of steep coast, as mentioned in Stettner et al. (2017).

Stettner et al. (2017) calculated 22-day coastline movements based on a threshold classification for an ice-rich riverbank situated in the Lena Delta. They used TerraSAR-X images from March 2013 to October 2015 and reported erosion estimates for 22-day intervals. Unlike Stettner's data, this study's data spans seven months (from July 2018 to January 2019), but almost all of the erosion would have occurred during the 41 days without sea ice. To compare this study's 41-day erosion estimates with Stettner's 22-day estimates, the calculated mean net change value (−0.01 m) of this study was multiplied by 22/41. Stettner's year-by-year results for 2013 to 2015 were -1.37 ± 1.55 m, -1.96 ± 1.85 m, and -1.85 ± 1.97 m per 22 days. This study's 2018 estimate of −0.01 m per 22 days indicates significantly less erosion.

However, the features in the region Stettner studied are different from the region studied here. The feature differences appear to explain the different erosion estimates. The Lena Delta (Stettner's study) is in a region with active cliff sections that undergo erosion and retrogressive thaw slumping (Stettner et al., 2017), so erosion processes are active. High resolution Péiades images from 2018-07-26 show that the area around Kay Point (this study) has high bluffs with no signs of recent erosion (Fig. 5.22), indicating that erosion processes near Kay Point are not very active. Therefore it is reasonable that the Kay Point erosion rate is lower than the Lena Delta estimate.

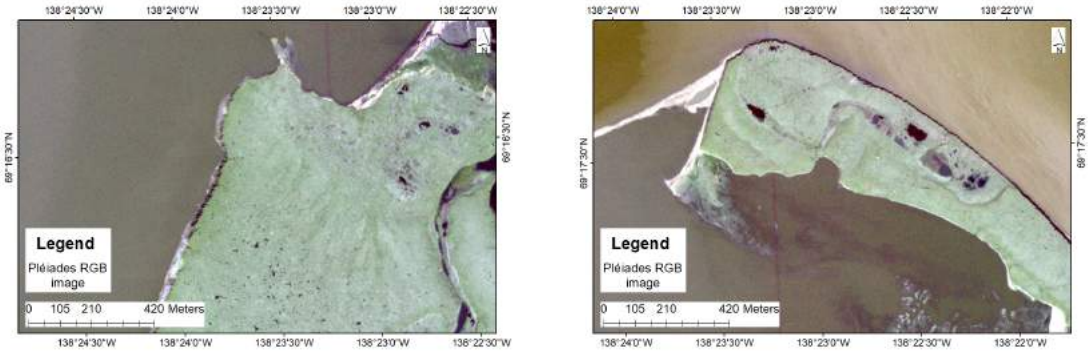

(a) Area 1 (b) Areas 2–4

FIGURE 5.22: Pléiades images taken 2018-07-26 of Kay Point Areas 1–4 show high bluffs with no signs of recent erosion.

5.2.2 Yukon Coast: Kay Point Annual Changes

In three areas of another region near Kay Point (Fig. 5.23), 43 of 72 transects showed coastline movement between 2007 and 2018. The average movement was 0.55 ± 1 m/year.

32.56% of the transects showed a coastline retreat, but no statistically significant erosion was observed. The maximum erosion rate of 2.18 m/year was observed in Area 1. The average erosion rate is 0.62 m/year. The accretion rates were significant in 13.95% of transects, and the average accretion rate was 1.1 m/year. The maximum accretion rate (3.14 m/year) was observed in Area 3. A result summary is given in Table 5.9.

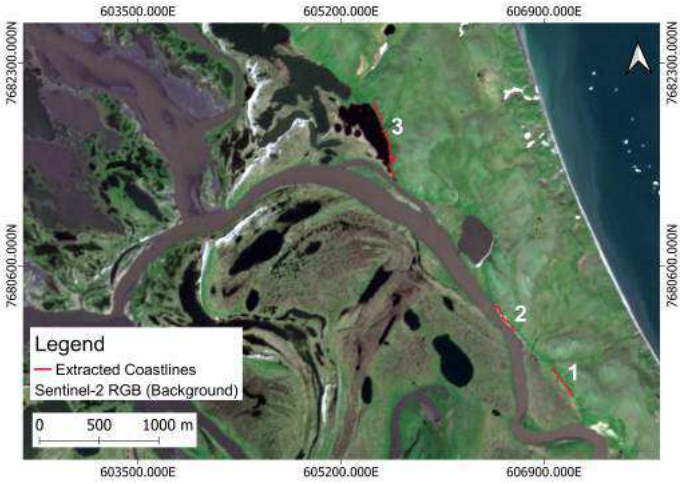

FIGURE 5.23: Yukon Coast shorelines extracted from 2007–2018 PALSAR and PALSAR-2 data with the three areas marked. The background is a Sentinel-2 RGB image.

Area	Coastline Type	Mean Change Rate m/year	Mean Erosion Rate m/year	Mean Accretion Rate m/year
1		0.54 ± 1.67	0.7	1.24
2	Cliff-Top	0.84 ± 2.18	0.32	0.99
3		0.34 ± 2.01	0.51	0.91

TABLE 5.9: Summary of the Kay Point annual shoreline movements calculated with PALSAR and PALSAR-2 image classifications. A mean change rate < 0 indicates erosion.

These results are similar to results published by Irrgang et al. (2018). Their study calculated shoreline movements of the Yukon Coast based on aerial and satellites images between the years 1951 and 2011. Their calculated movement rates for two areas close to this study area are -0.4 m and 0.0 m per year, which indicates that the accretion and erosion processes in this area are not very active.

5.2.3 Yukon Coast: Herschel Island Annual Changes

Shoreline change rates between the years 2007–2018 and 2017–2018 were calculated for the three areas on the west coast of Herschel Island marked in Fig. 5.24. The results are listed in Table 5.10.

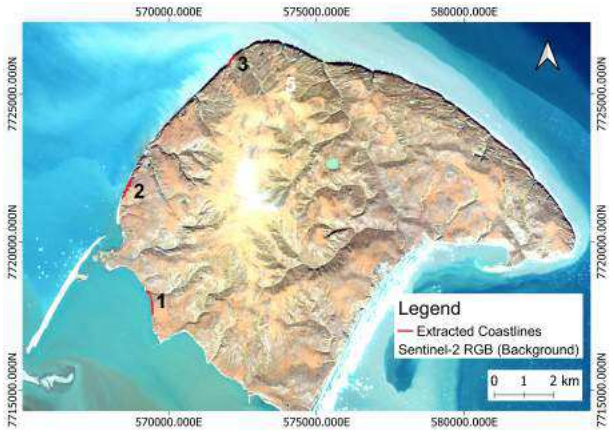

FIGURE 5.24: Herschel Island shorelines extracted from PALSAR, PALSAR-2, and Sentinel-1 data with the 3 areas marked. The background is a Sentinel-2 RGB image.

Sensor	Area	Coastline Type	Mean Change Rate m/year	Mean Erosion Rate m/year	Mean Accretion Rate m/year
P., P.-2	1	Cliff-Top	0.86 ± 0.75	0.89	1.17
P.		Cliff-Top	-3.12 ± 14.18	7.91	4.35
S.-1		Cliff-Top	0.54 ± 27.75	7.41	6.32
S.-1		Land–Water	-4.99 ± 28.68	13.22	13.25
P., P.-2	2	Cliff-Top	-2.22 ± 1.8	2.76	0.31
P.		Cliff-Top	4.76 ± 14.18	22.07	9.23
S.-1		Cliff-Top	5.78 ± 27.75	15.61	16.47
S.-1		Land–Water	-29.99 ± 28.68	33.59	9.57
P., P.-2	3	Cliff-Top	-1.91 ± 4.6	1.91	None
P.		Cliff-Top	-1.15 ± 14.18	10.03	4.51
S.-1		Cliff-Top	-2.33 ± 27.75	8.51	7.97
S.-1		Land–Water	27.76 ± 28.68	none	27.76

TABLE 5.10: Shoreline movement results calculated with PALSAR (P.), PALSAR-2 (P.-2) and Sentinel-1 (S.-1) images for Herschel Island. Rows with both PALSAR and PALSAR-2 data span 2007–2018. Other rows span 2017–2018. A mean change rate < 0 indicates erosion.

PALSAR and PALSAR-2, 2007–2018

In total, 100 segments were tested for changes, and 97 had undergone changes. The weighted linear regression calculated an average change rate of -0.83 ± 0.87 m/year for all segments. 13.98% of all segments show statistically significant erosion. The maximum value with 6.85 m/year can be found in the northern part of Area 3. The average erosion rate of all eroding segments is 2.24 m/year. 9.68% of all transects showed statistically significant accretion, with an average accretion rate of 1.04 m/year. The maximum accretion rate of 2.67 m/year was identified in Area 2. In general, in Area 1 accretion is more dominant, while in Areas 2 and 3 the erosion processes dominate as illustrated in Fig. 5.25.

Obu et al. (2016) used lidar elevation data from 2012 and 2013 with a horizontal resolution of 1 m to study short-term coastal erosion at the Yukon Coast including Herschel Island. Although they defined the coastline as land–water border instead of cliff top, the results for the northern part of Area 3 are consistent with this study. Their calculated coastline movement for these area is -6.8 m/year (Obu et al., 2016), which is similar to the results of this study (-6.85 m/year).

Comparing the results with the Péiades images from 2018-07-26, one can observe that the surfaces of Area 2 and 3 show signs of past erosion, while Area 1 seems to be relatively undisturbed. Thaw slumps are visible, especially in Area 2. This could explain the relatively high erosion rates observed in both this study and in Obu et al. (2016).

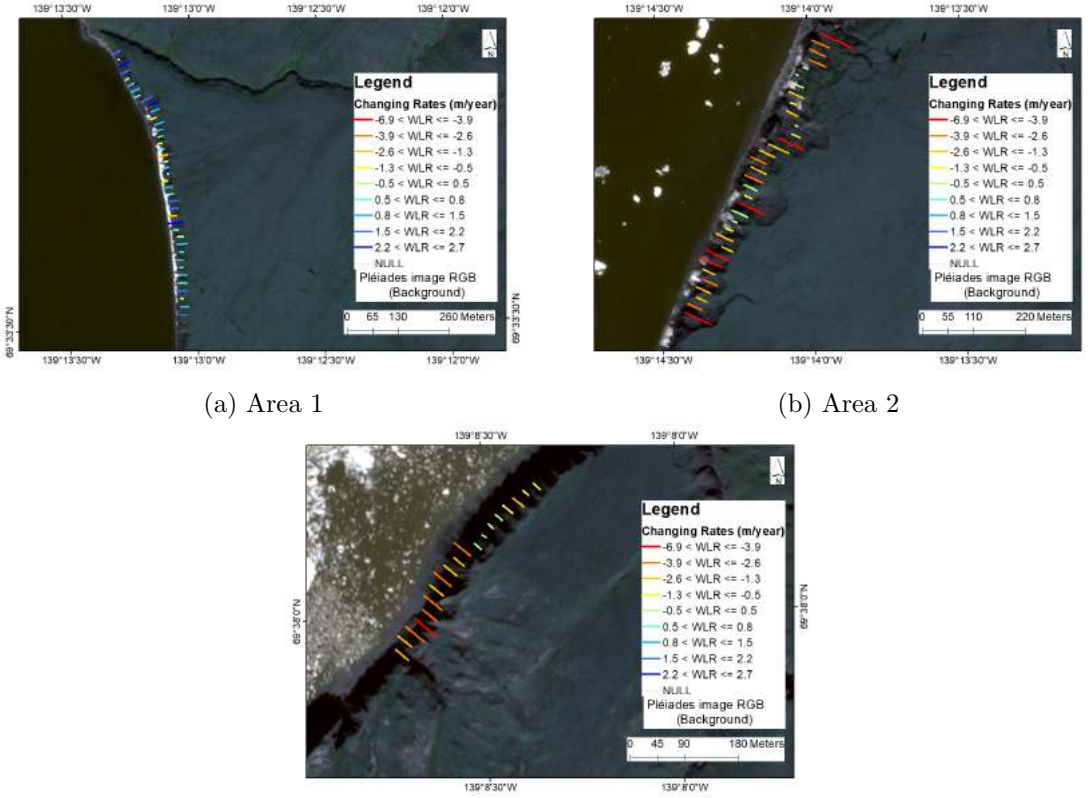

(a) Area 1

(b) Area 2

(c) Area 3

FIGURE 5.25: Transect-by-transect ten year coastal change rates of the west coast of Herschel Island. Red indicates erosion and blue indicates accretion. The background is a multispectral Pléiades image

PALSAR-2 and Sentinel-1, 2017–2018

Change rates for the 2017–2018 period were calculated from both Sentinel-1 and PALSAR-2 data. However, due to the offset between the Sentinel-1 and PALSAR-2 images, it was challenging to align cliff-top lines to compare the rates. 99 PALSAR-2 segments and 87 Sentinel-1 segments were tested for coastal changes. In total, 87 of 99 PALSAR-2 and 47 of 87 Sentinel-1 segments showed measurable movement.

The average change rates are similar for both satellites. The PALSAR-2 and Sentinel-1 rates were -0.18 ± 8.19 and 0.90 ± 16.02 m/year, respectively. The difference may be explained by the fact that the calculations assess slightly different areas. Due to their spatial resolution, the uncertainties are relatively high. 8.05% of the PALSAR-2 segments and 2.13% of the Sentinel-1 coastlines show statistically significant erosion rates. The average annual erosion rate calculated with PALSAR-2 is 9.9 m/year and with Sentinel-1 is 9.4 m/year, which is very similar. The accretion values of both are also similar: 7.16 m/year (PALSAR-2) and 7.18 m/year (Sentinel-1). The maximum accretion values of 37.49 m/year and 34.07 m/year of PALSAR-2 and Sentinel-1 are both

located in the same region in the north of Area 2. The maximum erosion values of 34.84 m/year and 32.04 m/year year of PALSAR-2 and Sentinel-1 calculated from both images are in the south of Area 2. The mean change rates in Area 2 are -3.12 ± 27.75 m/year (PALSAR-2) and 0.54 ± 28.68 m/year, and the difference could be caused by a cliff-top line gap in the Sentinel-1 data. The overall coastline change tendencies calculated with images from both sensors match. The calculated 2017–2018 changes for Area 2 were similar positive rates, even though the 2007–2018 result showed a negative trend. As mentioned before, Fig. 5.25b shows thaw slumps in this area. The difference between the short-term and long-term trends could be caused by the high uncertainty of the calculations based on 2017–2018 shorelines.

Sentinel-1 Descending, 2017–2018

Change rates were also calculated for the same area based on images from Sentinel-1 with an descending flight designation. In this case the land–water border was used as coastline, because the coast area of interest did not face the sensor. Across the 3 areas, 95 transects were tested for coastline movements, and 94 segments with coastline changes were found. The average coastline change rate is -9.28 ± 16.56 m/year, and therefore higher than the results based on cliff-top lines. 23.40% of the segments are eroding, with a mean erosion rate of 24.27 m/year. Statistically significant accretion took place in 4.26% of the segments, with a mean rate of 17.18 m/year. Those two rates are also higher than all of the calculated rates based on cliff-top lines.

The area-by-area land–water results are extremely different from the cliff-top results, especially in Areas 2 and 3. This could be caused by snow. The Pléiades image from 2018-07-26 (background RGB of Fig. 5.25) shows snow in Areas 2 and 3. The land–water approach seems to be affected by this snow more than the cliff-top calculations. This could be realistic because snow will last longer on a shaded wall or sand area than on top of the cliff where the sun shines more often. In Area 1 where no snow can be detected on the Pléidaes image, the results seem to match, regardless of ascending/descending flight designation.

Allowing for the high uncertainties of the calculated rates, the overall tendencies of the cliff-top line results calculated based on two and ten years match well. The approach based on the non-sensor-facing land–water border seems to be strongly affected by snow.

5.2.4 Bykovsky Peninsula

For the Bykovsky Peninsula, only ten year changes of the cliff-top lines could be calculated because no other data was available. However, the classification and extraction of

the cliff-top lines was more effective for the Bykovsky Peninsula than the other regions.

In total, 1028 transects in 6 areas were tested for shoreline movements. The locations of the 6 areas are marked in Fig. 5.26. Weighted linear regression calculated non-zero changes for 998 of the 1028 transects. The average annual change rate is -0.93 ± 0.29 m/year. Statistically significant accretion was observed at 3.51% of the transects. The average shoreline accretion rate is 0.83 m/year, and the maximum (5.53 m/year) is located in Area 3. Statistically significant erosion, with an average of 1.88 m/year, was observed for 14.83% of the transects. The highest erosion rate (10.01 m/year) was observed at a transect in Area 2. This area has on average the highest erosion rates (-5.22 m/year). Around 97% of the tested transects in this area are classified as eroding. Areas 3 to 6 show comparatively low mean change rates between -0.09 ± 0.61 and -0.75 ± 0.41. Area 1 has a positive change rate of 0.41 ± 0.54.

FIGURE 5.26: Bykovsky Peninsula shorelines extracted from PALSAR and PALSAR-2 data with the 6 areas marked. The background is a Sentinel-2 RGB image.

Area	Coastline Type	Mean Change Rate m/year	Mean Erosion Rate m/year	Mean Accretion Rate m/year
1	Land–Water	0.41 ± 0.54	0.75	1.01
2		-5.22 ± 0.94	5.54	0.9
3		-0.09 ± 0.61	0.71	0.62
4		-0.14 ± 1.76	0.78	0.56
5		-0.44 ± 1.00	0.79	0.55
6		-0.75 ± 0.41	1.29	0.80

TABLE 5.11: Summary of the Bykovsky Peninsula shoreline movements calculated with PALSAR and PALSAR-2 image classifications. A mean change rate <0 indicates erosion.

Coastal erosion dynamics on Bykovsky Peninsula were calculated between 1951 and 2006 by Lantuit et al. (2011). They analyzed airborne and spaceborne optical images and calculated the annual erosion rates. Like in this study, the highest coastal erosion rates on the west-coast were found in Area 2, with rates between 1.51 and 2 m/year. These rates are lower than the result of this study but indicate the same erosion pattern. They also show that the other areas are less affected by erosion, which is consistent with the result of this study (Lantuit et al., 2011).

5.2.5 Barents Sea Coast

The coastline of the Barents Sea Coast contains of many wide beaches, which were difficult to correctly classify as land. Furthermore, sand areas are often affected by tides, and it is difficult to distinguish tidal motion from erosion. Therefore the classification results were compared to Landsat 7 and Landsat 8 images, and an area with good match between the classification result and the images was chosen (Fig. 5.27). Because only a single area is evaluated, the relevant results are reported in the section summary (Table 5.7).

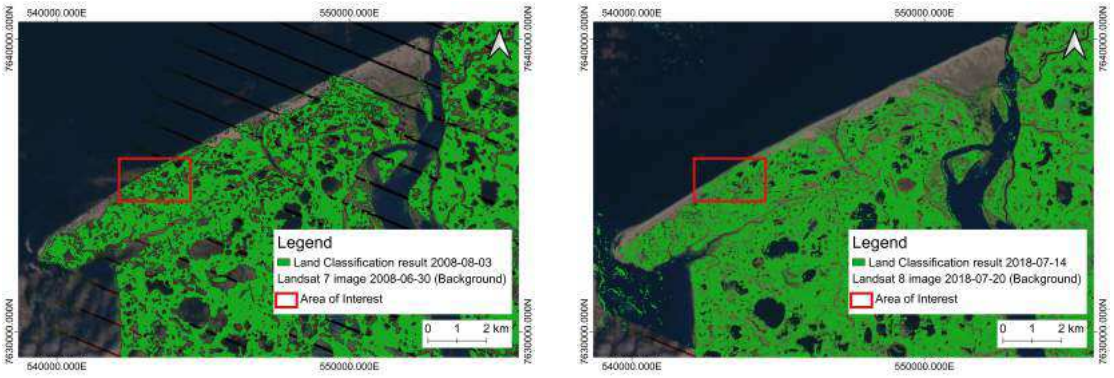

(a) PALSAR-2 land Classification. Background: Landsat 7 2008-08-28

(b) Sentinel-2 land classification. Background: Landsat 8 2018-07-20

FIGURE 5.27: Barents Sea coast classification result comparison with Landsat 7 and 8 images

PALSAR and PALSAR-2, 2007–2018

The weighed linear regression for the Barents Sea region shows high annual erosion rates. All 22 transects are affected by erosion processes, and 86.36% of the tested segments showed significant erosion rates. The average erosion rate is 5.41 ± 3.03 m/year, with a maximum rate at 8.29 m/year. Refer to the transect-by-transect erosion rates plotted in Fig. 5.28.

FIGURE 5.28: Ten year coastal change rates: Barents Sea Coast

PALSAR-2 and Sentinel-1, 2017–2018

The calculation of annual changes between 2017 and 2018 used 31 transects for each satellite. For Sentinel-1, 30 transects showed shoreline changes; for the PALSAR-2, only 21 transects. As mentioned before, the images of both satellites are not well aligned,

which made it difficult to align the coastline transects. Furthermore, the total Sentinel-1 coastline segment was slightly longer, because of a small gap in the PALSAR-2 coastline.

In general, both satellites show the same trends. The average coastal change rate calculated from PALSAR-2 images is -2.5 ± 17.55 m/year, while the rate calculated from Sentinel-1 images is -3 ± 28.68 m/year. The percentage of eroding coast segments is high for both satellites. 52% of the PALSAR-2 coastline transects and 70% of the Sentinel-1 transects were affected. The Sentinel-1 average erosion rate of -11.64 m/year is a bit higher than the value calculated with PALSAR-2 images (-9.53 m/year). Like the erosion averages, the Sentinel-1 results show a higher value (12.23 m) than the PALSAR-2 results (7.53 m). Interestingly, the maximum accretion value of both satellites occurs at the same transect with similar values of 20.49 m for Sentinel-1 and 20.36 m for PALSAR-2.

Leont'yev (2003) predicted that the open coast of Varandey would retreat 300 to 500 m over the next century, or 3 to 5 m/year. This study's calculated 2007–2018 erosion rate of 5.41 m/year is slightly faster Leont'yev's rate, but matches within the uncertainty. Surprisingly, the two-year rates calculated in this study were very close Leont'yev's rate, even though their uncertainties are still extremely large. As mentioned before, it is challenging to distinguish between tidal and wave motion and erosion processes in sand areas without vegetation or cliffs. The tidal motion can cause calculation errors.

5.3 Rate-of-Change Comparison

The mean change rates of the Herschel Island and Barents Sea Coasts based on 2017–2018 shorelines were plotted against the change rates based on 2007–2018 shorelines in Fig. 5.29. No correlation between the rates is apparent. This could be caused by the high uncertainty value of the 2017–2018 results or changes of the erosion and accretion processes over time. The results based on descending Sentinel-1 images (triangle markers) show a completely different trend than the other values. The PALSAR-2 and Sentinel-1 rates based on cliff-top lines seem to agree, except for the mean change rate at Herschel Island in Area 3 (red x and circle markers). As mentioned before, this could be caused by a gap in the Sentinel-1 cliff-top line.

It would be interesting to compare change rates based on 2007–2018 C-band data with the calculated rates based on 2007–2018 PALSAR/PALSAR-2 L-band data. Unfortunately, only coarse resolution (30 m) data for the areas of interest are available for ENVISAT (the predecessor satellite of Sentinel-1)(ESA, 2019a). Future studies could include data from the operationally focused Canadian RADARSAT-2 satellite. Images

with a higher resolution than 30 m are available for some study areas (e.g. Herschel Island) between 2008–2019 (MDA, 2019).

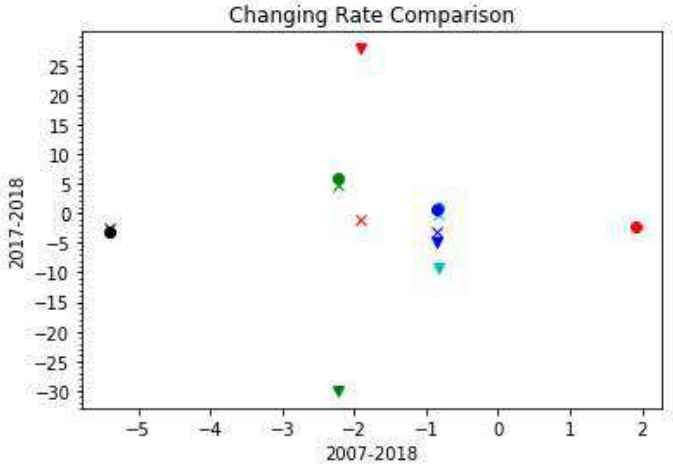

FIGURE 5.29: Comparison of the calculated two-year mean change rates (vertical axis) and the ten year rates (horizontal axis). Rates were calculated at all Areas of Herschel Island (cyan), Barents Sea (black), and Herschel Island Areas 1 (blue), 2 (green) and 3 (red). Calculations are based on PALSAR-2 cliff-top lines (x marker), Sentinel-1 cliff-top lines (circle marker), and Sentinel-1 land–water border (triangle marker).

A comparison of the mean erosion and accretion rates based on cliff-top lines derived from PALSAR-2 and Sentinel-1 images between 2017–2018 (Fig. 5.30) shows a correlation between the results. Ideally, the trend would line up with $y = x$. The deviation from $y = x$ could be explained by the high uncertainty of the change rates (caused by the low spatial resolution of the images) and possible small differences between the chosen transects and the orbit parameter of the compared images.

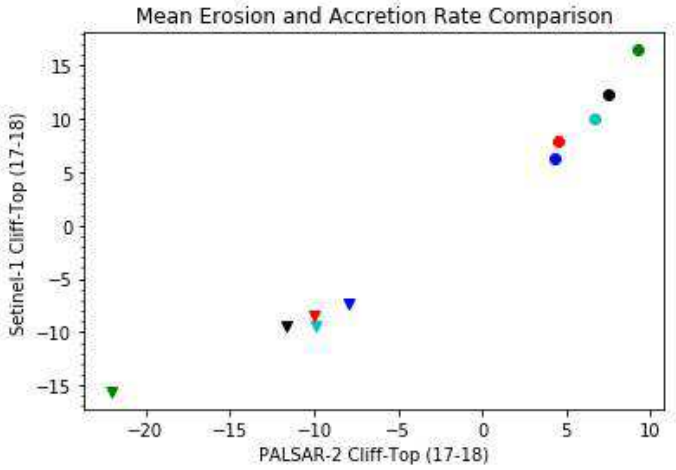

FIGURE 5.30: Comparison of the calculated mean accretion and erosion rates based on PALSAR-2 (horizontal axis) and Sentinel-1 (vertical axis) cliff-top lines from 2017–2018. The rates of all Areas of Herschel Island (cyan) and Barents Sea Coast (black), and Herschel Island Areas 1 (blue), 2 (green), and 3 (red) are shown. Erosion rates (triangle markers) and accretion rates (circle markers) are both shown.

6. Conclusion

This study demonstrates the use of threshold classification to monitor coastal erosion in these regions. In this study, filtered and unfiltered high-resolution TerraSAR-X X-band, and lower resolution Sentinel-1 C-band and PALSAR/PALSAR-2 L-band images were used. A threshold classification method was generated to automatically classify steep coasts, land, and water surfaces in different arctic environments. Based on samples, two incidence-angle dependant thresholds for each satellite were calculated to identify these surfaces.

The analysis of the effect of the incidence angle on the backscatter showed only weak influences. The distributions of the steep coast, land, and water samples were best explained with linear threshold functions. This is true for unfiltered and filtered samples and for all sensors. Only small differences were found between the sample distribution of samples from Sentinel-1 images with descending and ascending flight designation, and between PALSAR and PALSAR-2 samples. Therefore, the ascending and descending Sentinel-1 samples were used together to derive the threshold functions. For the PALSAR and PALSAR-2 threshold calculation only PALSAR-2 samples were used, because of their higher spatial resolution. During the error assessment all steep-coast test-samples were successfully classified as steep coast by the threshold functions. In general, the threshold functions for filtered, co-polarized images had a slightly higher classification accuracy, with κ between 83.52 and 99.84%. The only exception was the threshold functions for Sentinel-1 images, which showed severe scalloping. Here the thresholds based on unfiltered images had a slightly higher accuracy (95.94%) than the threshold based on filtered images (95.32%). The threshold functions for the TerraSAR-X images showed the best performance, and the PALSAR/PALSAR-2 threshold had the worst performance.

The comparison of the classification results with optical data revealed three main issues: snow, wide sand beaches, and infrastructure. In the classification results, wet snow was misclassified as water, which made classifications during snow melt difficult. In future work, including a threshold function to determine snow melt may help avoid possible misclassifications.

Classification is also complicated by smooth sand beaches. The sand backscatter values of long-wave C-band and L-band microwaves are relatively low, which made a distinction between water and sand challenging. Future studies may overcome this challenge by introducing a third threshold function between sand and water.

Infrastructures also caused misclassifications. Houses had high backscatter values and were misclassified as steep coast. However, this was only an issue when infrastructure was located directly at steep coast.

The classification results were used to calculate shoreline movements at the Yukon Coast and Bykovsky Peninsula based on the steep coast classifications. The boundary between the land and water classifications was used for shoreline movement calculations in regions were no steep coast could be observed. This was the case at the Barents Sea Coast with flat sand beaches and the west coast of Herschel Island that was facing away from the satellites with a descending flight designation.

Seasonal changes in a region near Kay Point (Yukon Coast) showed a low shoreline change rate of -0.01 m per 22-days. No signs of recent erosion could be seen on the optical Pléiades images from 2018-07-26, which indicates that this result could be reasonable. The same is true for calculated annual shoreline change rates near that region. Based on cliff-top lines extracted from PALSAR/PALSAR-2 steep coast classifications between 2007–2018, a small change rate of 0.55 ± 1.00 m/year was calculated. Comparison with optical images and previous studies confirms that the erosion and accretion processes in this region are not very active.

For the west coast of Herschel Island, the calculated long-term (2007–2018) mean change rates based on PALSAR/PALSAR-2 steep coast classifications (-0.83 ± 0.87) show good accordance with the short-term (2017–2018) mean change rates based on PALSAR-2 (-0.18 ± 8.19) and Sentinel-1 (0.9 ± 16.02) steep coast classifications.

When the land–water border of the Sentinel-1 classifications was used, the mean change rate was much lower (-9.28 ± 16.56). A reason for this could be snow, because the high-resolution Pléiades images that were captured around the same time show snow in the areas where result differences occurred.

The mean change results of the west coast of Bykovsky Peninsula calculated with the steep coast classifications based on PALSAR/PALSAR-2 images from 2007–2018 revealed that in most of the areas, small rates of change took place (-0.75–0.41 m/year). Only Area two had a high change rate of -5.22 m/year. This is consistent with the erosion and accretion trends shown in a previous study based on optical images.

At the Barents Sea Coast it was challenging to find a coast area with good accordance between the classification result and optical images. Also, the definition of the coastline was difficult, because there are only beaches in that area, which could be affected by tidal motion. The resulting mean change rates calculated based PALSAR/PALSAR-2 between 2007–2018 (-5.41 ± 3.03), and PALSAR-2 and Sentinel-1 images between 2017–2018 (-2.51 ± 17.55, -3.00 ± 28.68) are similar to the erosion trend of 3 m/year predicted in a previous study.

Greater differences between the short- and long-term result become apparent when the erosion and accretion rates of Herschel Island and the Barents Sea Coast are split into smaller areas. One reason for this could be the high uncertainty of the calculated short-term values or a change in the erosion and accretion processes. Comparing the results of the PALSAR-2 and Sentinel-1 short-term calculations based on steep coast classifications shows a positive correlation. However, the calculated rates are not identical. This could be explained by the low resolution of the images and possibly by small differences between the chosen transects and the orbit parameters of the compared images.

In general, the calculation of long-term shoreline movements of sensor facing steep coasts in the Arctic based on a threshold classification seems to be a promising approach. The calculated rates based on PALSAR/PALSAR-2 L-band images between 2007–2018 seem to bring reasonable results. However, for the prediction of short-term trends based on low-resolution Sentinel-1 and PALSAR-2 images, the uncertainties are high. This may be improved by using more than one image per year. Another limitation of the low resolution is that only erosion features equal to or greater than the resolution of the image can be detected.

A comparison of the PALSAR/PALSAR-2 L-band long-term results of this study with RADARSAT-2 C-band long-term results would be an interesting research field for future studies. Also, the calculation of seasonal trends with TerraSAR-X data in a region with more active erosion would be interesting. The threshold based method can help to better understand the seasonal, annual, and inter-annual Arctic coastline dynamics, and it provides additional information that complements the optical and in situ methods.

References

Airbus (2015). TerraSAR-X Image Product Guide. Basic and Enhanced Radar Satellite Imagery. Technical report.

Albertz, J. (2009). *Einführung in die Fernerkundung*. WBG.

Antonova, S., Duguay, C. R., Kääb, A., Heim, B., Langer, M., Westermann, S., and Boike, J. (2016). Monitoring Bedfast Ice and Ice Phenology in Lakes of the Lena River Delta Using TerraSAR-X Backscatter and Coherent Time Series. *Remote Sensing*, 8(903).

Arp, C. D., Jones, B. M., Schmutz, J. A., Urban, F. E., and Jorgenson, M. T. (2010). Two mechanisms of aquatic and terrestial habitat change along an Alaskan Arctic coastline. *Polar Biol*, 33:1629–1640.

ASF (2019). MapReady. `https://www.asf.alaska.edu/data-tools/mapready`. Version 3.1.24.

Astrium (2012). *Pléiades Imagery User Guide*, second edition.

Baghdadi, N., Pedreros, N., Lenotre, N., Dewez, T., and Paganini, M. (2007). Impact of polarization and incidence of the SAR sensor on coastline mapping: example of Gabon. *International Journal of Remote Sensing*, 28(17):3841–3849.

Balz, T. and Liao, M. (2010). Building-damage detection using post-seismic high-resolution SAR satellite data. *International Journal of Remote Sensing*, 31(13).

Banks, S. N., King, D. J., Merzouki, A., and Duff, J. (2014). Assesing RADARSAT-2 for Mapping Shoreline Cleanup and Assesment Technique (SCAT) Classes in the Canadian Arctic. *Canadian Journal of Remote Sensing*, 40(3):243 – 267.

Barnhart, K. R., Overeem, I., and Anderson, R. S. (2014). The effect of changing sea ice on the physical vulnerability of Arctic coasts. *The Cryosphere*, 8:1777–1799.

Bartsch, A., Pointner, G., Leibman, M. O., Dvornikov, Y. A., Khomutov, A. V., and Trofaier, A. M. (2017). Circumpolar Mapping of Ground-Fast Lake Ice. *Frontiers in Earth Science*, 5:12.

Bartsch, A., Widhalm, B., Pointner, G., Ermokhina, K., Leibman, M., and Heim, B. (2019). Landcover derived from Sentinel-1 and Sentinel-2 satellite data (2015-2018) for subarctic and arctic environments.

Couture, N. J., Irrgang, A., Pollard, W., Lantuit, H., and Fritz, M. (2018). Coastal Erosion of Permafrost Soils Along the Yukon Coastal Plain and Fluxes of Organic Carbon to the Canadian Beaufort Sea. *Journal of Geophysical Research: Biogeosciences*, 123:406–422.

Cunliffe, A. C., Tanksi, G., Radosavljevic, B., Palmer, W. F., Sachs, T., Lanuit, H., Kerby, J. T., and Myers-Smith, I. H. (2019). Rapid retreat of permafrost coastline observed with aerial drone photogrammetry. *The Cryosphere*, 13:1513–1528.

ESA (2007). Information on ALOS PALSAR Products for ADEN users. Technical report.

ESA (2012). Sentinel-1. ESA's Radar Observatory Mission for GMES Operational Services. Technical report.

ESA (2015). Sentinel-2 User Handbook. Technical report.

ESA (2019a). ESA Online Catalogue. `http://esar-ds.eo.esa.int/socat/ASA_IMP_1P`. [Online; accessed 01-September-2019].

ESA (2019b). Sentinel Application Platform (SNAP). `http://step.esa.int/main/toolboxes/snap`.

Frederick, J. M., Thomas, M. A., Bull, D. L., Jones, C. A., and Roberts, J. D. (2016). The Arctic Coastal Erosion Problem. Technical report, Sandia National Laboratories.

French, H. M. (2008). *The Periglacial Environment*. Wiley, third edition.

Government Canada (2019). Historical Climate Data. `http://climate.weather.gc.ca/historical_data/search_historic_data_e.html`. [Online; accessed 15-July-2019].

Grosse, G., Schirrmeister, L., Kunitsky, V. W., and Hubberten, H.-W. (2005). The use of CORONA images in Remote Sensing of Periglacial Geomorphology: An Illustration from the NE Sibirian Coast. *Permafrost and Periglacial Processes*, 16:163–172.

Guégan, E., Sinitsyn, A., Kokin, O., and Ogorodov, S. (2016). Coastal Geomorphology and Ground Thermal Regime of the Varandey Area, Northern Russia. *Journal of Coastal Research*, 32(5):1025–1031.

Günther, F., Overduin, P. P., Sandakov, A. V., Grosse, G., and Grigoriev, M.-N. (2013). Short- and long-term thermo-erosion of ice-rich permafrost coasts in the Laptev Sea region. *Biogeosciences*, 10:4297–4318.

Himmelstoss, E. A., Henderson, R. E., Kratzmann, M. G., and Farris, A. S. (2018). *Digital Shoreline Analysis System (DSAS). Version 5.0 User Guide*. USGS.

Hinzman, L. D., Bettez, N. D., Bolton, W. R., Chapin, F. S., Dyurgerov, M. B., Fastie, C. L., Griffith, B., Hollister, R., Hope, A., Huntington, H. P., Jensen, A. M., Jia, G. J., Jorgenson, T., Kane, D. L., Klein, D. R., Kofinas, G., Lynch, A. H., Lloyd, A. H., McGuire, A. D., Nelson, F. E., Oechel, W. C., Osterkamp, T. E., Racine, C. H., Romanovski, V. E., Stone, R. S., Stow, D. A., Sturm, M., Tweedie, C. E., Vourlitis, G. L., Walker, M. D., Walker, D. A., Webber, P. J., Welker, J. M., Winker, K. S., and Yoshikawa, K. (2005). Evidence and Implications of Recent Climate Change in Northern Alaska and Other Arctic Regions. *Climate Change*, 72:251–298.

Hoque, M. A. and Pollard, W. H. (2004). Modeling block failures of vertical cliffs in the Arctic Coast. *Arctic Coastal Dynamic. Report of the 5th International Workshop*, pages 60–64.

Hoque, M. A. and Pollard, W. H. (2009). Arctic coastal retreat through block failure. *Canadian Geotechnical Journal*, 46(10):1103–1115.

Irrgang, A. M., Lantuit, H., Manson, G. K., Günther, F., Grosse, G., and Overduin, P. P. (2018). Variability in Rates of Coastal Change Along the Yukon coast, 1951 to 2015. *Journal of Geophysical Research: Earth Surface*, 123(4):779–800.

JAXA (2008). *ALOS Data Users Handbook. Revision C.*

JAXA (2018). *ALOS-2 Solution Book. Proposals for 'DAICHI 2' SAR Data Utilization.* Third edition.

Jensen, J. R. (2005). *Introductory Digital Image Processing. A Remote Sensing Perspective*. Pearson Education, Inc., third edition.

Jones, B., Hinkel, K. M., Arp, C. D., and Eisner, W. R. (2008). Modern Erosion Rates and Loss of Coastal Features and Sites, Beaufort Sea Coastline, Alaska. *Arctic*, 61(4):361–372.

Jones, G. H. and Vaughan, R. A. (2010). *Remote Sensing of Vegetation. Principles, Techniques and Applications*. Oxford.

Kroon, A. (2014). *Coastal Environments and Global Change*, chapter 14. High-Latitude Coasts, pages 338–353. John Wily & Sons.

Lantuit, H. (2008). *The modification of arctic permafrost coastlines*. PhD thesis, Universität Potsdam.

Lantuit, H., Atkinson, D., Overduin, P. P., Grigoriew, M., Rachold, V., Grosse, G., and Hubberten, H.-W. (2011). Coastal erosion dynamics on the permafrost-dominated Bykovsky Peninsula, north Siberia, 1951-2006. *Polar Research*, 30(7341).

Lantuit, H., Overduin, P. P., Couture, N., Wetterich, S., Aré, F., Atkinson, D., Brown, J., Cherkashov, G., Drozdov, D., Forbes, D. L., Graves-Gaylord, A., Grigoriev, M., Hubberten, H.-W., Jordan, J., Jorgenson, T., Ødegård, R. S., Ogorodov, S., Pollard, W. H., Rachold, V., Sedenko, S., Solomon, S., Steenhuisen, F., Streletskaya, I., and Vasiliev, A. (2012). The Arctic Coastal Dynamics Database: A New Classification Scheme and Statistics on Arctic Permafrost Coastlines. *Estuaries and Coasts*, 35(2):383–400.

Lantuit, H. and Pollard, W. H. (2008). Fifty years of coastal erosion and retrogressive thaw slump activity on Herschel Island, southern Beaufort Sea, Yukon Territory, Canada. *Geomorphology*, 95(1):84 – 102.

Le, T. M. H., Depina, I., Guegan, E., and Sinitsyn, A. (2018). Thermal regime of permafrost at Varandey Settlement along the Barents Sea Coast, North West Arctic Russia. *Engineering Geology*, 246:69–81.

Lee, J.-S., Wen, J.-W., Ainsworth, T. L., Chen, K.-S., and Chen, A. (2009). Improved Sigma Filter for Speckle Filtering of SAR Imagery. *IEEE Transactions on Geoscience and Remote Sensing*, 47(1):202–213.

Leont'yev, I. O. (2003). Modeling erosion of sedimentary coasts in the western Russian Arctic. *Coastal Engineering*, 47:413–429.

MDA (2019). MDA's RADARSAT-2 Portal. `https://mdacorporation.com/geospatial/international/radarsat-portal`. [Online; accessed 01-September-2019].

NASA (1989). Instrument Panel Report. SAR: Synthetic Aperture Radar. Earth Observation System Vol.iif. Technical report, NASA.

Obu, J., Lantuit, H., Grosse, G., Günther, F., Sachs, T., Helm, V., and Fritz, M. (2016). Coast erosion and mass wasting along the Canadian Beaufort Seas based on annual airborne LiDAR elevation data. *Geomorphology*, 293:331–346.

Obu, J., Westermann, S., Kääb, A., and Bartsch, A. (2018). Ground Temperature Map, 2000-2016, Northern Hemisphere Permafrost.

Overland, J., Dunlea, E., Box, J. E., Corell, R., Forsius, M., Kattov, V., Olsen, M. S., Pawlak, J., Reiersen, L.-O., and Wang, M. (2018). The Urgency of Arctic Change. *Polar Science*.

Pointner, G. (2019). Python Code for Vector to Polygon Coversion. Personal Communication.

Radosavljevic, B., Lantuit, H., Pollard, W., Overduin, P., Couture, N., Sachs, T., Helm, V., and Fritz, M. (2016). Erosion and Flooding Threats to Coastal Infrastructure in the Arctic: A Case Study from Herschel Island, Yukon Territory, Canada. *Estuaries and Coasts*, 39:900–915.

Romanovsky, V. E., Smith, S. L., and Christiansen, H. H. (2010). Permafrost thermal state in the polar northern hemisphere during the international polar year 2007–2009: a synthesis. *Permafrost and Periglac. Process*, 21:106–116.

Romeiser, R., Horstmann, J., Caruso, M. J., and Graber, H. C. (2013). A Descalloping Postprocessor for ScanSAR Images of Ocean Scenes. *IEEE Transactions on Geoscience and Remote Sensing*, 51(6):3259–3272.

Schlaffer, S., Chini, M., Dettmering, D., and Wagner, W. (2016). Mapping Wetland in Zambia Using Seasonal Backscatter Signatures Derived from ENVISAR ASAR Time Series. *Remote Sensing*, 8(402).

Schubert, A., Miranda, N., Geudtner, D., and Small, D. (2017). Sentinel-1A/B Combined Product Geolocation Accuracy. *Remote Sensing*, 9(6).

Shimada, M. (2009). Advance Land-Observation Satellite (ALOS) And Its Follow-On Satellite, ALOS-2.

Solomon, S. M. (2005). Spatial and temporal variability of shoreline change in the Beaufort-Mackenzie region, northwest territories, Canada. *Geo-Marine Letters*, 25(2):127–137.

Steele, M., Ermold, W., and Zhang, J. (2008). Arctic Ocean surface warming trends over the past 100 years. *Geophysical Research Letters*, 35.

Stephen, H. and Long, D. G. (2005). Microwave Backscatter Modeling of Erg Surfaces in the Sahara Desert. *IEEE Transactions on Geoscience and Remote Sensing*, 43(2).

Stettner, S., Beamish, A., Bartsch, A., Heim, B., Grosse, G., Roth, A., and Lantuit, H. (2017). Monitoring Inter- and Intra-Seasonal Dynamics of Rapidly Degrading Ice-Rich Permafrost Riverbanks in the Lena Delta with TerraSAR-X Time Series. *Remote Sensing*, 10(1).

Stettner, S., Lanuit, H., Heim, B., Eppler, J., Roth, A., Bartsch, A., and Rabus, B. (2018). TerraSAR-X Time Series Fill a Gap in Spaceborne Snowmelt Monitoring of Small Arctic Catchments–A Case Study on Qikiqtaruk (Herschel Island), Canada. *Remote Sensing*, 10(1155).

Strozzi, T., Antonova, S., Günther, F., Mätzler, E., Vieira, G., Wegmüller, U., Westermann, S., and Bartsch, A. (2018). Sentinel-1 SAR Interferometry for Surface Deformation Monitoring in Low-Land Permafrost Areas. *Remote Sensing*, 10(9).

Ullmann, T., Banks, S. N., Schmitt, A., and Jagdhuber, T. (2017). Scattering Characteristics of X-, C- and L-Band polSAR Data Examined for the Tundra Environment of the Tuktoyaktuk Peninsula, Canada. *Applied Sciences*, 7(595).

USGS (2018). Landsat 7 (L7) Data Users Handbook. Technical Report 1, Department of the Interior U.S. Geological Survey.

USGS (2019). Landsat 8 (L8) Data Users Handbook. Technical Report 4, Department of the Interior U.S. Geological Survey.

Wang, L., Marzahn, P., Bernier, M., Jacome, A., Poulin, J., and Ludwig, L. (2017). Comparison of TerraSAR-X and ALOS PALSAR Differential Interferometry With Multisource DEMs for Monitoring Ground Displacement in a Discontinuous Permafrost Region. *IEEE Journal of Selected Topics in Applied Earth Observations and Remote Sensing*, 10(9):4074–4093.

Woodhouse, I. H. (2006). *Introduction to Microwave Remote Sensing*. CRC Press.

Zwieback, S., Kokelj, S., Boike, J., Grosse, G., and Hajnsek, I. (2017). Sub-seasonal thaw slump mass wasting is not consistently energy limited at the landscape scale. *The Cryosphere Discuss*, pages 1–24.